Solar Physics
DOI: 10.1007/•••••-•••-•••-••••-•

Wavelength Dependence of the *Helioseismic and Magnetic Imager* Instrument

Sébastien Couvidat[1] · **Jesper Schou**[1] · **Richard A. Shine**[2] · **Rock I. Bush**[1] · **John W. Miles**[3] · **Philip H. Scherrer**[1] · **Richard L. Rairden**[2]

Received: 29 December 2009/ Revised: 7 January 2011

Abstract The *Helioseismic and Magnetic Imager* (HMI) instrument will produce Doppler-velocity and vector-magnetic-field maps at the solar surface, whose accuracy is dependent on a thorough knowledge of the transmission profiles of the components of the HMI optical-filter system. Here we present a series of wavelength dependence calibration tests, performed on the instrument from 2005 onwards, to obtain these profiles. We obtained the transmittances as a function of wavelength for the tunable and non-tunable filter elements, as well as the variation of these transmittances with temperature and the angle of incidence of rays of light. We also established the presence of fringe patterns produced by interferences inside the blocking filter and the front window, as well as a change in transmitted intensity with the tuning position. This thorough characterization of the HMI filter system confirmed the very high quality of the instrument, and that its properties are well within the required specifications to produce superior data with high spatial and temporal resolution.

Keywords: Sun: helioseismology, Instrument: SDO/HMI

1. Introduction

The *Helioseismic and Magnetic Imager* instrument (HMI; see Scherrer *et al.*, 2010, for a general presentation of HMI, and Schou *et al.*, 2010, for a general presentation of its calibration) onboard the *Solar Dynamics Observatory* satellite

[1] W.W. Hansen Experimental Physics Laboratory
491 S Service Road, Stanford University
Stanford, CA 94305-4085, USA
email: couvidat@stanford.edu
[2] Lockheed Martin Solar and Astrophysics Laboratory
Bldg. 252, Org. ADBS, 3251 Hanover Street
Palo Alto, CA 94304, USA
[3] USRA / SOFIA, NASA Ames Research Center, Moffett
Field, CA 94035, USA

(SDO; see Pesnell *et al.*, 2010) makes measurements, in the absorption line Fe I centered at the in-air wavelength 6173.3433 Å (hereafter the target wavelength; *e.g.* Norton *et al.*, 2006; Dravins, Lindegren, and Nordlund, 1981), of the motion of the solar photosphere to study solar oscillations, and of the polarization to study all three components of the photospheric magnetic field. HMI samples the neutral iron line at (nominally) six positions (hereafter sampling positions) symmetrical around the line center at rest. Each sampling-position transmission profile must be as close to a delta function as possible: to this end, HMI is built around an optical-filter system composed of a front window, a blocking filter, a five-stage Lyot filter, and two Michelson interferometers. This system produces a narrow bandpass transmission profile, or transmittance, with a nominal Full Width at Half Maximum [FWHM] of 76 mÅ and a nominal FWHM of 612 mÅ for the non-tunable (fixed) part. The knowledge of the transmittance of each element constituting the optical-filter system is required to access the characteristics of the HMI sampling positions (especially their transmission profile as a function of wavelength), and thus to derive accurate Doppler velocities and vector magnetic fields from the corresponding filtergrams. The term filtergram refers to a picture of the Sun obtained through a specific sampling position, *i.e.* at a specific wavelength, and polarization. From December 2005 to August 2009, the assembled instrument has been subjected to many tests, whose purpose was twofold: first, to detect any defect before launch; second, to calibrate the instrument.

In this paper we present the calibration of the wavelength dependence of HMI: this is the process by which we characterize the components of the HMI optical-filter system in terms of their transmittances and how these transmittances are affected by temperature, angle of incidence of the rays of light, change of focus blocks, and so on. In Section 2 we remind the reader of the theoretical transmittances of the Lyot elements, of the Michelson interferometers, and of the origin of interference fringes produced by the front window and blocking filter on the HMI filtergrams. In Section 3 we present the main calibration results: wavelength, angular, and thermal dependences. In Section 4 we present other calibration results, *e.g.* thermal stability and instrument throughput, and also preliminary plans for on-orbit calibration. We conclude in Section 5.

2. Theoretical Wavelength Dependence

The core of the HMI instrument is its optical-filter system, composed of a front window, a blocking filter, a five-stage Lyot filter, and two Michelson interferometers. The blocking filter, Lyot filter, and Michelson interferometers are enclosed in a temperature-stabilized oven. The requirement for the oven stability is $\pm 0.01^{\circ}$C/h, but the actual performance is better. The nominal operating oven temperature is 30° C. In this section we derive the theoretical transmittances of the filter elements. The layout of HMI is presented on Figure 1. HMI can operate in two main modes: OBSMODE and CALMODE. In CALMODE, the instrument aperture is imaged instead of the Sun, and therefore the front window is in focus. CALMODE is used only for calibration purpose, while OBSMODE is used during normal operations.

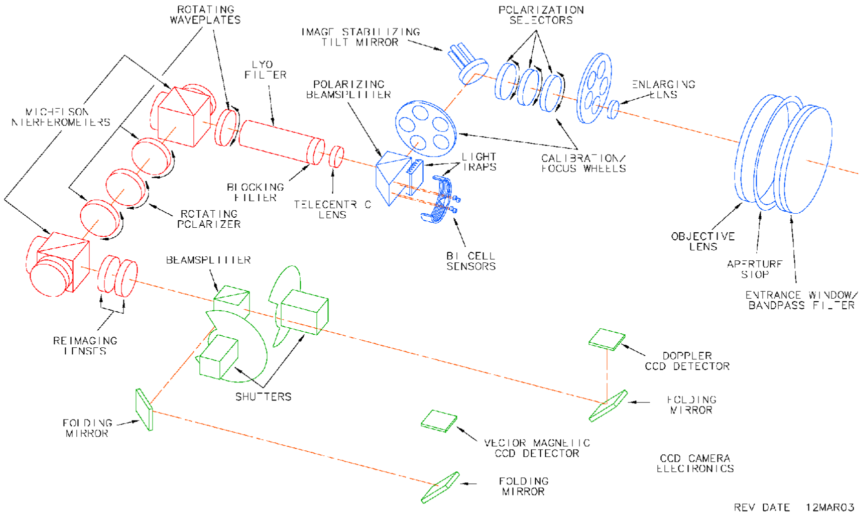

Figure 1. Layout of the HMI instrument. The optical-filter system is drawn in red.

2.1. Lyot Filter

The HMI Lyot filter is a five-element wide-field (hereafter WF) tunable birefringent filter. These elements (stages) are referred to as E2, E3, E4, E5, and E1 (in order of appearance from the blocking filter to the wide-band Michelson interferometer). The narrowest element E1 (in terms of the FWHM of its transmittance) is made tunable by the addition of a rotating half-wave plate at the exit. The other wave plates are fixed. A telecentric lens at the entrance of the filter oven produces a collimated beam for the Lyot filter: the angular distribution of light is identical for each image point. In order to minimize the temperature sensitivity of the filter, we used the same basic design employed for the SOHO/MDI instrument (Scherrer et *al.*, 1995). Therefore, each Lyot element is made of two birefringent crystals: calcite and either ADP (Ammonium Dihydrogen Phosphate) or KDP (Potassium Dihydrogen Phosphate). KDP is used for the thinner elements E4 and E5 because the necessary ADP thicknesses are too small to be easily fabricated. ADP/KDP crystals are used in combination with calcite to cancel out the wavelength change with temperature of the calcite crystals.

2.1.1. Time Delay

A birefringent crystal decomposes a ray of light into two rays propagating at different velocities: the ordinary and extraordinary rays. Uniaxial birefringent crystals (crystals with a single optical axis) such as calcite, ADP, and KDP are therefore characterized by two refractive indices: n_e for the extraordinary axis (parallel to the optical axis) and n_o for the ordinary axis (perpendicular to the

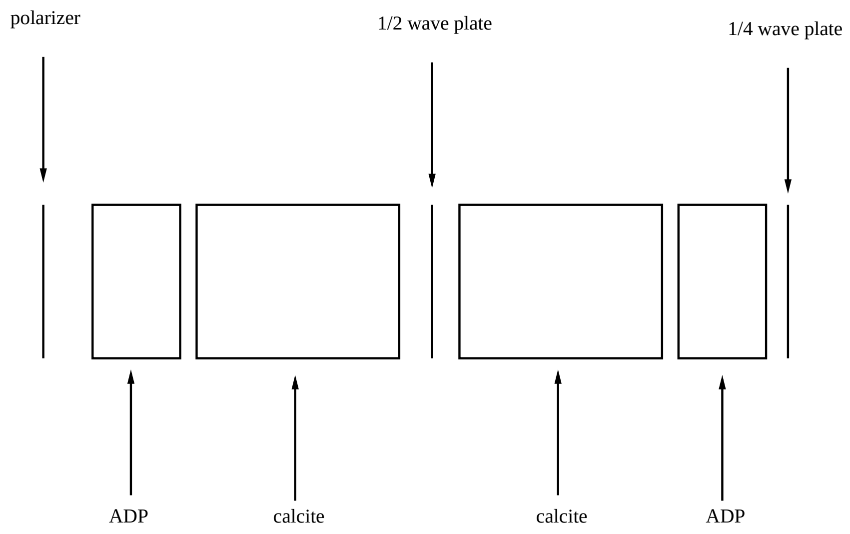

Figure 2. Exploded view of the Lyot element E1. Light enters through the polarizer and exits through the quarter-wave plate. The tuning half-wave plate is not shown, but is located behind the quarter-wave plate.

Table 1. Properties of optical crystals used in HMI at wavelength $\lambda = 6173$ Å and temperature $T_e = 25°$ C. The values of the refractive indices n_e and n_o are derived from Sellmeier's equations, with the coefficients taken from the United Crystals and AD Photonics websites (www.unitedcrystals.com/KDPProp.html and www.adphotonics.com/products/calcite_specifications.pdf). The change in birefringence [Δn] with wavelength is $\alpha = \partial \Delta n / \partial \lambda$. The thermal expansion coefficients $\alpha_{\shortparallel} = (1/d)\, \partial d / \partial T_e$, where d is the length of the element, are taken from the Quantumtech website (quantumtech.com/PDF/702.PDF).

Crystal	n_o	Δn	α (Å^{-1})	$\frac{\partial \Delta n}{\partial T}$ (°C^{-1})	$\alpha_{\shortparallel}$ (°C^{-1})
calcite	1.65656	−0.1707	3.2592 10^{-6}	9.98 10^{-6}	5.68 10^{-6}
ADP	1.52311	−0.0396	1.2679 10^{-6}	5.23 10^{-5}	4.20 10^{-6}
KDP	1.50780	−0.0394	1.2530 10^{-6}	1.43 10^{-5}	44.0 10^{-6}

optical axis). The birefringence of such a crystal is defined as $\Delta n = n_e - n_o$. Some optical and physical properties of calcite, ADP, and KDP are listed in Table 1. Some physical properties of the five temperature-compensated, WF-Lyot elements are listed in Table 2, while Figure 2 shows an exploded view of the element E1. Note that, except for the extra ADP (or KDP) elements, this

Table 2. Nominal lengths of the Lyot stages of HMI (mm). (A) refers to ADP, (K) to KDP. The FSRs are nominal (FSR_n) full spectral ranges in mÅ at 6173 Å. $\partial\lambda/\partial T_e$ is the measured wavelength shift with temperature, in mÅ°C^{-1}, around 30°C. Δn_1 and Δn_2 are the birefringences, and d_1 and d_2 are the crystal lengths. The index 1 refers to the Calcite crystal, while 2 refers to either ADP or KDP.

Element	Calcite	ADP/KDP	$\lvert d_1\Delta n_1 - d_2\Delta n_2\rvert$	FSR_n	$\partial\lambda/\partial T_e$
E1	30.620	7.056 (A)	4.89561	690	-3.06
E2	15.310	3.528 (A)	2.44781	1380	-1.36
E3	7.655	1.764 (A)	1.22390	2758	-4.10
E4	4.662	4.500 (K)	0.61451	5516	6.87
E5	2.330	2.250 (K)	0.30725	11032	10.04

is the usual design of a WF-Lyot element as discussed in detail by Title and Rosenberg (1979).

The on-axis time delay of a WF element that is not temperature-compensated is the same as the time delay of a simple Lyot element with the same total thickness of birefringent material, but the angular dependence is greatly reduced. The time delay [Δt] between the ordinary and extraordinary rays is:

$$\begin{aligned}\Delta t \; = \; & \frac{D}{2c}\left\{ n_e\left[1-\left(\frac{a^2}{{n_o}^2}+\frac{b^2}{{n_e}^2}\right)\right]^{1/2} - n_o\left[1-\left(\frac{a^2+b^2}{{n_o}^2}\right)\right]^{1/2}\right\} \\ & +\frac{D}{2c}\left\{ n_e\left[1-\left(\frac{a'^2}{{n_o}^2}+\frac{b'^2}{{n_e}^2}\right)\right]^{1/2} - n_o\left[1-\left(\frac{a'^2+b'^2}{{n_o}^2}\right)\right]^{1/2}\right\} \qquad (1)\end{aligned}$$

where:

$$a = \sin(\theta)\cos(\phi), \quad b = \sin(\theta)\sin(\phi) \qquad (2)$$

and

$$a' = \sin(\theta)\cos(\phi+\pi/2), \quad b' = \sin(\theta)\sin(\phi+\pi/2) \qquad (3)$$

Here θ is the angle between the ray and the optical axis (angle of incidence), while ϕ is the azimuthal angle. Note that n_e and n_o are functions of wavelength and temperature. c is the speed of light. Finally, D is the total thickness of both calcite components separated by the half-wave plate (again, we ignore the ADP or KDP components for the present) and the two major terms are for these two calcite components. The ϕ terms cancel, and when expanding out to second order in θ, the angular dependence near the axis (*i.e.* for small θ) reduces to:

$$\Delta t \approx \frac{D}{c}(n_e - n_o)\left[1 - \frac{\theta^2}{4{n_o}^2}\left(\frac{n_e-n_o}{n_e}\right)\right] \qquad (4)$$

This results in a relative wavelength shift in the off-axis directions of:

$$\frac{\delta\lambda}{\lambda} \approx -\frac{\theta^2}{4{n_o}^2}\left(\frac{n_e - n_o}{n_e}\right) \tag{5}$$

which should be compared with the simple Lyot (not WF) results of:

$$\begin{aligned} \left.\frac{\delta\lambda}{\lambda}\right|_{\phi=0} &\approx -\frac{\theta^2}{2{n_o}^2}, \\ \left.\frac{\delta\lambda}{\lambda}\right|_{\phi=\frac{\pi}{2}} &\approx +\frac{\theta^2}{2n_o n_e} \end{aligned} \tag{6}$$

at the two indicated azimuthal angles (Title and Rosenberg, 1979). For the calcite components, the improvement of a WF design in angular dependence is about a factor of eleven in either of these directions, with the additional advantage of no azimuthal dependence.

Along the axis ($\theta = 0$) we have:

$$\Delta t \approx \frac{D(n_e - n_o)}{c} = \frac{D\Delta n}{c} \tag{7}$$

Taking into account the presence of ADP or KDP blocks paired with calcite in the HMI Lyot stages, the total theoretical delay for a normal ray becomes:

$$\Delta t \approx \frac{d_1\Delta n_1 - d_2\Delta n_2}{c} \tag{8}$$

where d_1 and d_2 are the total lengths of, respectively, calcite and ADP (or KDP), while Δn_1 and Δn_2 are their birefringences.

2.1.2. Wavelength Dependence

At $\theta = 0$ the retardance $\Gamma(\lambda, \theta)$ for a calcite WF element is:

$$\Gamma(\lambda, 0) = \frac{2\pi c\Delta t}{\lambda} \approx \frac{2\pi D\Delta n}{\lambda} \tag{9}$$

The corresponding transmittance $T(\lambda, \theta)$ is (Evans, 1949):

$$T(\lambda, 0) = \cos^2\left(\frac{\Gamma(\lambda, 0)}{2}\right) = \frac{1 + \cos(\Gamma(\lambda, 0))}{2} \tag{10}$$

which can be approximated as:

$$T(\lambda, 0) \approx \frac{1 + \cos(2\pi\lambda/\mathrm{FSR})}{2} \tag{11}$$

where FSR is the free spectral range (defined and calculated in the next section).

The on-axis transmittance modeled by Equation (11) is for the ideal case of a perfect Lyot element. Actual Lyot stages in HMI have defects, *e.g.* misalignments and/or imperfect retardances of waveplates or polarizer, and to account for some of these defects their transmittance at $\theta = 0$ is modeled as:

$$T(\lambda, 0) = \frac{1 + B\cos(2\pi\lambda/\mathrm{FSR} + \Phi)}{2} \tag{12}$$

where B is the contrast of the element, and Φ is its relative phase. A contrast smaller than one and a gradient in the relative phase across the aperture indicate a defect. For the tunable element E1, the potential presence of an I-ripple (variation in the transmitted intensity as a function of the tuning position; see Section 2.4) is ignored in this model. Characterizing the Lyot elements wavelength dependence entails determining the values of $\mathrm{B}(x, y)$ and $\Phi(x, y)$ at every location (x, y) on the HMI CCD(s) and for the specific distribution of angles of incidence inside HMI, as well as determining the FSRs of the different elements.

2.1.3. Free Spectral Range

The Free Spectral Range [FSR] of a filter element is defined as the wavelength separation between the peaks of maximum transmittance. From Equation (9) it is clear that for a constant Δn this would approximately be:

$$\mathrm{FSR} \approx \left|\frac{2\pi\lambda}{\Gamma(\lambda)}\right| \approx \left|\frac{\lambda^2}{D\Delta n}\right|, \tag{13}$$

the more exact formula from Evans (1949) is:

$$\mathrm{FSR} \approx \left|\frac{\lambda^2}{D\Delta n}\left(1 - \frac{\lambda}{\Delta n}\frac{\partial \Delta n}{\partial \lambda}\right)^{-1}\right| \tag{14}$$

As discussed by Title (1974), the extra term makes about a 10% difference for visible wavelengths.

2.1.4. Thermal Compensation

The transmission peaks of a calcite Lyot element shift with temperature due to a combination of thermal expansion and a change in Δn. This shift is independent of the element thickness and Title *et al.* (1976) give the following formula based on experimental data:

$$\begin{aligned}\frac{\partial\lambda}{\partial T_e} &= (1 + 5.88\times 10^{-8}\lambda T_e)\times \\ &\quad (1.711\times 10^{-3} - 3.126\times 10^{2}\lambda^{-1} + 6.86\times 10^{-5}\lambda - 7.55\times 10^{-10}\lambda^2)\end{aligned} \tag{15}$$

where T_e is the temperature in °C and λ is in Å. For the Fe I line at the target wavelength and at the planned operating temperature of 30°C, the wavelength shift is 0.35Å°C^{-1}.

This temperature dependence can be greatly reduced by adding retarding crystals to each side of the WF element in such a way as to cancel out the calcite wavelength shift $\partial\lambda/\partial T_e$. ADP and KDP crystals have a smaller birefringence but a larger value of $\partial\lambda/\partial T_e$. Unfortunately, the derivatives are of the same sign, meaning that we have to add the ADP/KDP components in subtraction (*i.e.*, with their fast axis rotated by 90° relative to the calcite's fast axis). Therefore, the two calcite components in a WF Lyot element including ADP (or KDP) components are thicker than the calcite components of a Lyot element with no extra crystals but the same FSR.

The condition for thermal compensation at a specific wavelength λ is:

$$\partial(d_1\Delta n_1 - d_2\Delta n_2)/\partial T_e = 0 \tag{16}$$

which implies that we can make $\partial\lambda/\partial T_e$ vanish at the target wavelength and $T_e =$ 30°C for any element thickness with the proper choice of d_1/d_2. We determined the optimum values of $R_{\mathrm{ADP}} = d_1/d_{\mathrm{ADP}}$ and $R_{\mathrm{KDP}} = d_1/d_{\mathrm{KDP}}$ experimentally by fabricating sets of ADP and KDP crystals with thicknesses that gave us our estimated R_{ADP} and R_{KDP}, plus thicknesses about 5% higher and lower. Using a spectrograph, the transmission profile of each calcite–ADP and calcite–KDP pair (enclosed in an oven) was measured from 25 to 35°C. Then, $\partial\lambda/\partial T_e$ was fit by a second-order polynomial and the slope at 30°C was computed. The results are shown in Figure 3. The final ratios R_{ADP} and R_{KDP} for a zero wavelength shift were then determined by fitting a straight line to the three values in each set. The results are: $R_{\mathrm{ADP}} = 4.339$, $R_{\mathrm{KDP}} = 1.036$, and the calcite thicknesses must be increased by factors of, respectively, 1.056 and 1.286, compared with the basic WF design with no ADP/KDP crystals. Note that even the 5% error cases show a $\partial\lambda/\partial T_e$ value much lower than the 0.35Å/°C value for calcite alone. The actual measured values of $\partial\lambda/\partial T_e$ for each of the five elements before assembly are shown in Table 2.

Fortunately, the additional ADP/KDP crystals do not greatly affect the angular performance of the WF design but do degrade it slightly, mostly because of the increased thickness of the calcite components compared to a calcite-only design with the same FSR. With the addition of ADP/KDP crystals, Equation (5) becomes:

$$\frac{\delta\lambda}{\lambda} \approx -\frac{\theta^2}{4{n_{o_1}}^2}\left(\frac{n_{e_1}-n_{o_1}}{n_{e_1}}\right)\left[\frac{d_1}{D} - \frac{d_2}{D}\frac{{n_{o_1}}^2}{{n_{o_2}}^2}\frac{{\Delta n_2}^2}{{\Delta n_1}^2}\frac{n_{e_1}}{n_{e_2}}\right] \tag{17}$$

where we have factored out the equivalent calcite result and the terms in the square brackets represent the effect of the temperature-compensating components. D is the total thickness of the calcite components for the corresponding calcite-only design. n_{o_1} and n_{e_1} are the refractive indices for calcite, while n_{o_2} and n_{e_2} are the refractive indices for ADP/KDP. For the calcite+ADP design, $\delta\lambda/\lambda$ is increased by a factor 1.041 compared to calcite-only, and for the calcite+KDP design it is increased by 1.206. The d_1/D term (the necessary increase in calcite thickness) is the dominant factor.

2.2. Michelson Interferometers

The HMI Michelson interferometers are located after the beam-control lens placed at the end of the Lyot filter (see Figure 1). They are outside the telecentric

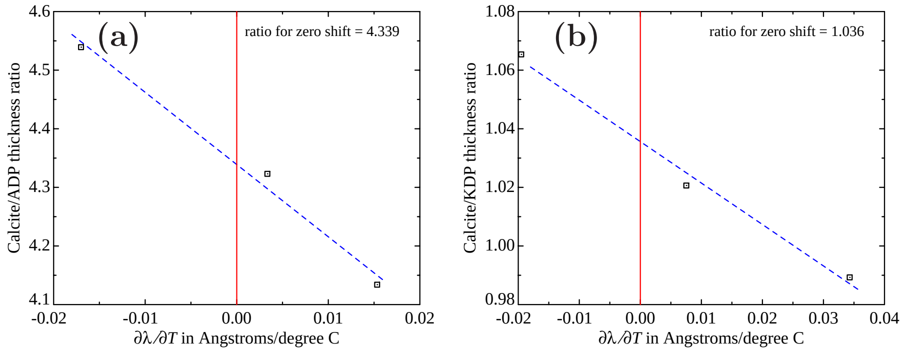

Figure 3. Thickness ratios for the crystals used in the Lyot filter as a function of the temperature dependence of the transmission profile. (a) The squares are the measured $\partial\lambda/\partial T_e$ values for a calcite crystal (9.26 mm thick) and three ADP crystals with different thicknesses intended to span the $\partial\lambda/\partial T_e = 0$ condition. The dashed line is a linear fit and the intersection with the vertical line at zero gives the optimal ratio d_1/d_2 (see text). (b) Same for the KDP case using a calcite crystal 2.77 mm thick.

beam, meaning the chief rays are not parallel to the optical axis anymore. A consequence is that the angular distribution of light is not identical at each image point: the rays reaching a specific point on the CCD are distributed in a cone-shaped beam inside the optical filter, and different image points in the Michelsons will have different diameters and distributions of angles of incidence. Similarly to the Lyot elements, the two Michelson interferometers are WF. Compared to a standard Michelson interferometer, a glass block (here made of N-BK7 optical glass) is added to one of the legs, and the Michelson is made tunable through the addition of a half-wave plate placed outside the interferometer and not through movable mirrors. Moreover, an entrance polarizer, a polarizing beamsplitter, an output quarter-wave plate and two mirror quarter-wave plates are also added to the usual Michelson design (see an exploded view on Figure 4).

2.2.1. Time Delay

The optical-path difference $[\Delta(\theta)]$ as a function of angle of incidence $[\theta]$ through a Michelson interferometer is (Gault, Johnston, and Kendall, 1985):

$$\Delta(\theta) = 2(n_1 d_1 - n_2 d_2) - \left(\frac{d_1}{n_1} - \frac{d_2}{n_2}\right)\sin^2\theta - \left(\frac{d_1}{n_1^3} - \frac{d_2}{n_2^3}\right)\frac{\sin^4\theta}{4} - \left(\frac{d_1}{n_1^5} - \frac{d_2}{n_2^5}\right)\frac{\sin^6\theta}{8} \tag{18}$$

where n_1 and n_2 are the refractive indices of, respectively, the solid leg (note that n_1 depends on λ and T_e) and the vacuum leg ($n_2 = 1$ in vacuum), and d_1 and d_2 are the corresponding leg lengths. The WF condition is $d_1/n_1 = d_2/n_2$, because, in this case, the $\sin^2\theta$ term is canceled and:

$$\Delta(\theta) = 2(n_1 d_1 - n_2 d_2) - \left(\frac{d_1}{n_1^3} - \frac{d_2}{n_2^3}\right)\frac{\sin^4\theta}{4} - \left(\frac{d_1}{n_1^5} - \frac{d_2}{n_2^5}\right)\frac{\sin^6\theta}{8} \tag{19}$$

The time delay $[\Delta t]$ is related to the optical-path difference by $\Delta t = \Delta(\theta)/c$.

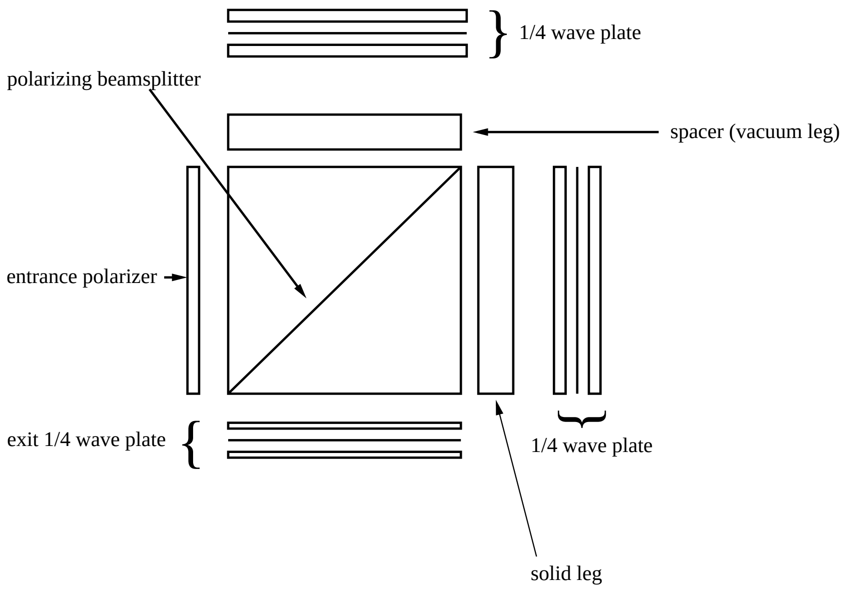

Figure 4. Exploded view of the wide-band HMI Michelson interferometer. The narrow-band Michelson is built the same way, but the light enters through the "exit" quarter-wave plate and exits through the "entrance" polarizer. The tuning half-wave plate is not shown.

2.2.2. Wavelength Dependence

From the optical-path difference we derive the retardance $\Gamma(\lambda,\theta) = 2\pi\Delta(\theta)/\lambda$ and the transmittance $T(\lambda,\theta)$ (Title and Ramsey, 1980):

$$T(\lambda,\theta) = \cos^2\left(\pi\frac{\Delta(\theta)}{\lambda} + 2\phi\right) = \frac{1+\cos\left(2\pi\frac{\Delta(\theta)}{\lambda} + 4\phi\right)}{2} \tag{20}$$

where ϕ is the tuning angle, *i.e.* the angle of the fast axis of the tuning half-wave plate to the fast axis of the output quarter-wave plate. We added the tuning angle in the equation of the transmittance of the Michelsons, and not in the equation of the transmittance of the Lyot elements (Equations (11) and (12)), because both Michelsons are tunable while only the Lyot element E1 is. Note that Equation (20) differs from Equation (11) of Title and Ramsey (1980) because in HMI the tuning is done by half-wave plates and not polarizers (the polarization axis is rotated twice as fast with a half-wave plate).

A non-zero incidence angle produces a theoretical wavelength change of only about 0.3 mÅ for a collimated beam at $\theta = 1.75°$ (half angle for the HMI field of view) and at target wavelength, if the WF compensation is perfectly achieved. However the WF condition does not hold at wavelengths different from the target one, because the condition $(1/n_1)\,\partial n_1/\partial\lambda = (1/n_2)\,\partial n_2/\partial\lambda$ is not valid for all λ since the vacuum leg has a constant refractive index.

Following section 2.1.2, the transmittance of a tunable Michelson at $\theta = 0$ can be expressed as:

$$T(\lambda, 0) \approx \frac{1 + \cos(2\pi\lambda/\mathrm{FSR} + 4\phi)}{2} \tag{21}$$

where the FSR is calculated in the next section. However the actual Michelson interferometers in HMI have imperfections (*e.g.* transmission and reflection coefficients smaller than one for the beam splitter, potentially incorrect retardances for the wave plates, misalignement of these wave plates, and so on), also the wavelength dependence of their transmittance at $\theta = 0$ is modeled as follows:

$$T(\lambda, 0) = \frac{1 + B\cos(2\pi\lambda/\mathrm{FSR} + \Phi + 4\phi)}{2} \tag{22}$$

where, as with the Lyot elements, B is the contrast and Φ is the relative phase, and both vary across the aperture. As previously mentioned, this simple transmittance model ignores any potential I-ripple (see Section 2.4).

In HMI, the peak transmittances of the two Michelson interferometers are expected to coincide for $\phi_2 = 2\phi_1$, where the index 1 refers to the Wide-Band (WB) Michelson and 2 refers to the Narrow-Band (NB) Michelson. This relation stems from $\Delta_2 = 2\Delta_1$ because the nominal FSR of the WB Michelson (344 mÅ) is twice that of the NB Michelson (172 mÅ).

The following relation gives the change $\delta\lambda$ in central wavelength of the transmission profile as a function of the change $\delta\phi$ in the angle of the tuning half-wave plate:

$$\delta\lambda = \frac{\mathrm{FSR}}{\pi} 2\delta\phi \tag{23}$$

The *modus operandi* to cotune the instrument is that the NB Michelson will be tuned by $\delta\phi = 36°$ steps (*i.e.* 24 Hollow-Core Motor [HCM] steps: one HCM step is 1.5°). The WB Michelson will be tuned by $\delta\phi = 18°$ (or 12 HCM steps). Finally, E1 will be tuned by $\delta\phi = 9°$ (or 6 HCM steps). Therefore, the tuning positions, *i.e.* sampling positions, will nominally be spaced by 68.8 mÅ.

2.2.3. Free Spectral Range

For a normal ray ($\theta = 0$) the FSR of a Michelson interferometer can be approximated as:

$$\mathrm{FSR} \approx \frac{\lambda^2}{\left|\Delta(\theta) - \lambda\frac{d\Delta(\theta)}{d\lambda}\right|} \tag{24}$$

We can further simplify this equation by assuming that $\Delta(\theta)$ does not depend on λ, and we obtain:

$$\mathrm{FSR} \approx \frac{\lambda^2}{|\Delta(\theta)|} \tag{25}$$

The FWHM, like for the Lyot elements, is equal to:

$$\mathrm{FWHM} \approx \frac{\mathrm{FSR}}{2} \tag{26}$$

2.2.4. Thermal Compensation

The Michelson interferometers are also thermally compensated: the vacuum leg is maintained with temperature-compensating copper standoffs. The “Stonehenge” design of the copper spacers reduces stress. This temperature compensation produces, to lowest order, a theoretical zero-sensitivity to temperature variation.

2.3. Front Window and Blocking Filter

The blocking filter is an interference filter made of two glass substrates and three cavities acting like Fabry-Perot interferometers and located in between the substrates. Its nominal FWHM is 8 Å, and it is centered close to the target wavelength (the center depends on the distribution of angles of incidence and of the temperature). The front window is made of three blocks of glass: a 6-mm thick Schott BK7 glass block, a 3-mm thick colored Schott GG495 glass block, a coating, and another 6-mm thick Schott BK7 glass block. Unwanted interferences arise inside the front window and blocking filter: they are engendered in the glass blocks, which, because of partial reflections at their interfaces, also act like weak Fabry-Perot interferometers. These interferences produce a fringe pattern visible on HMI filtergrams and which needs to be characterized. These fringes contaminate the phase and contrast maps of the other filter elements as determined by the calibration procedures, and they move with temperature. This will be a problem after the regular eclipses that HMI will be subjected to due to the geosynchronous orbit of SDO: after such events, the spatially-averaged temperature and the temperature gradient on the front window will need a certain time to stabilize.

2.3.1. Time Delay

In a Fabry-Perot interferometer placed in vacuum, the phase difference $\Delta\Phi$ between two consecutive reflections in a glass block of thickness d is:

$$\Delta\Phi(\lambda,\theta) = \frac{2\pi}{\lambda}\, 2\, n\, d \cos(\theta) \tag{27}$$

where θ is the angle of incidence of the rays measured inside the cavity and n is the refractive index of the glass between the two reflecting surfaces. The time delay [Δt] is the optical-path difference [$\Delta(\theta)$], with $\Delta(\theta) = 2\, n\, d \cos(\theta)$, divided by the speed of light.

2.3.2. Wavelength and Angular Dependences

The transmittance [$T(\lambda,\theta)$] of a Fabry-Perot cavity where the two surfaces have a reflectance R is given by:

$$T(\lambda,\theta) = \frac{(1-R)^2}{1+R^2-2R\cos(\Delta\Phi(\lambda,\theta))} \tag{28}$$

Neglecting the change in n with wavelength and using Equation (27), the Fabry-Perot cavity placed in vacuum has the following angular dependence, expressed in term of wavelength change $\delta\lambda$:

$$\delta\lambda \approx \lambda\left(\sqrt{1-\left(\frac{1}{n}\right)^2 \sin^2(\theta')} - 1\right) \tag{29}$$

where θ' is the angle of incidence measured outside the cavity (the Snell-Descartes law states that $n\,\sin(\theta) = \sin(\theta')$).

The blocking filter operates as a Fabry-Perot cavity that is crossed by a beam of rays of light covering a range of θ' angles. Also, following the recommendation of the blocking filter manufacturer, the Andover Corporation, the filter overall angular dependence can be approximated as (see www.andovercorp.com):

$$\delta\lambda \approx \frac{\lambda}{2}\left(\sqrt{1-\left(\frac{n_e}{n}\right)^2 \sin^2(\theta')} - 1\right) \tag{30}$$

where θ' is the maximum angle of incidence, λ is the central wavelength of the transmission profile at $\theta' = 0$, n is the effective refractive index of the filter cavity, n_e is the refractive index of the external medium, and Andover Corporation calculated $n_e/n = 1/2.05$. Compared to Equation (29), the factor $1/2$ is used to approximate the impact of a beam versus a single ray, while the ratio n_e/n expresses the fact that the external medium may have a refractive index different from 1. This equation is a good approximation for a beam of light with a maximum incidence angle $\theta' < 20°$, which is exactly the kind of beams crossing the blocking filter in HMI.

2.3.3. Free Spectral Range

From Equation (27), the FSR of a Fabry-Perot cavity is, in a first approximation (neglecting the change in n with wavelength):

$$\mathrm{FSR} \approx \frac{\lambda^2}{2\,n\,d\cos(\theta) + \lambda} \tag{31}$$

There is an implicit temperature dependence, as, for instance, the thickness of the glass block varies with T_e.

2.3.4. Thermal Compensation

There is no specific thermal compensation mechanism in the front window and blocking filter.

2.4. *I*-ripple

When taking a sequence of filtergrams in white light (*e.g.* with a lamp as source) we observe a variation in the transmitted intensity measured on the HMI CCDs from one sequence position to another. This variation is called an *I*-ripple. A small amount of *I*-ripple, expressed as the relative peak-to-peak difference of spatially-averaged intensities measured on the CCDs, is inevitable even for a perfect instrument: the integral values of the transmission profiles of the sequence positions are different, mainly because of the presence of the blocking filter and front window (which limit the wavelength range). In case of a perfect instrument with a blocking filter centered at the target wavelength and with a Gaussian transmission profile, the amount of *I*-ripple expected is of the order of a couple of tenths of a percent, at most.

Unfortunately, imperfections in the instrument increase this *I*-ripple. Possible causes of an *I*-ripple for a Lyot element include: error in the retardance of the half-wave plate; misalignement of the half-wave plate (which is difficult to detect and is the most likely cause of an *I*-ripple produced by E1); misalignement of both the entrance polarizer and the exit quarter-wave plate, misalignement of the entrance polarizer and retardation error in the tuning half-wave plate, and so on. Possible causes of an *I*-ripple for a Michelson interferometer include: a misalignment of both the entrance polarizer and the exit quarter-wave plate, an imperfection in the polarizing beamsplitter (*e.g.* polarization leaks) and a misalignement of the exit quarter-wave plate, a misalignment of the entrance polarizer and a retardation error in the tuning half-wave plate, and so on.

Jones calculus applied to a tunable Lyot element (A. Title, private communication, 2009) shows that its transmittance $T(\lambda,0)$ in presence of an imperfect half-wave plate can be modeled, in a second-order approximation, as:

$$T(\lambda,0) = K_0\,\frac{1+\cos(2\pi\lambda/\mathrm{FSR}+4\phi)}{2} + \frac{1}{2}(K_1\cos(2\phi)+K_2\sin(2\phi))^2 \qquad (32)$$

where the constants K_1 and K_2 are related to, respectively, the retardance error and the misalignement (tilt) of the half-wave plate, while $K_0 = 1-K_1^2/2-K_2^2/2$. The transmitted intensity I at a given position of a white-light sequence in which only the Lyot element is tuned can be approximated as:

$$\frac{I}{\bar{I}} = K_0 + (K_1\cos(2\phi)+K_2\sin(2\phi))^2 \qquad (33)$$

where $\bar{I}$ is the transmitted intensity averaged over a period of the tuning angles ϕ. To account for other imperfections in the tunable Lyot element, we could generalize its transmittance as:

$$T(\lambda,0) = K_0\,\frac{1+B\cos(2\pi\lambda/\mathrm{FSR}+4\phi+\Phi)}{2} + \frac{1}{2}(K_1\cos(2\phi)+K_2\sin(2\phi))^2 \qquad (34)$$

where Φ is the relative phase, and B is related to the contrast B of the element. Computing the Jones matrices characterizing defects, other than an imperfect half-wave plate, in the Lyot element E1 and in the Michelson interferometers shows that Equation (33) is a very good approximation for *I*-ripples produced in most cases studied, but Equation (34) is valid only for a Lyot element with an imperfect half-wave plate and is a more-or-less good approximation in all other cases.

3. Measured Wavelength Dependence

3.1. Calibration Hardware

Until November 2007, calibration tests were performed in a cleanroom at the Lockheed Martin Solar and Astrophysics Laboratory (LMSAL) facilities, in Palo Alto (California), then at the NASA Goddard Space Flight Center (Maryland), and finally after July 2009 at Astrotech Space Operations (Florida). Different light sources were used to feed HMI: the Sun through a heliostat, a dye laser (massive tunable laser using organic dye), a tunable infrared laser operated around 1234 nm (frequency-doubled using a periodically-poled lithium-niobate crystal, and assembled at Stanford University), and a lamp to provide white light (with a flat spectrum in the narrow wavelength range of interest). A stimulus telescope (the reversed HMI telescope) was used with the laser and lamp sources, so that the rays of light entering HMI have angles and trajectories similar to the ones HMI will encounter once SDO is launched. A diffuser was added when using the laser sources. Several field and aperture stops were also used. The field stop most often utilized was a solar-size stop (24.6 mm in diameter): placed at the focal plane of the stimulus telescope, it roughly provides the same incidence-angle distribution as the Sun. For the angular-dependence test, a small field stop (5 mm in diameter) was used. Calibration tests were performed both in air and in vacuum. For the tests performed in air, an air-to-vacuum corrector was sometimes added to the system and the stimulus telescope was despaced. In order to keep the CCDs cold and thereby reduce the dark current, a vacuum chamber was needed for some tests (cooling down in air is not possible due to condensation). Among other impacts, the phases [Φ] of the Michelson interferometers differ in air and vacuum. Before the instrument was fully assembled, isolated elements of the optical-filter system were also tested separately at LMSAL using additional devices, *e.g.* spectrographs. Table 3 summarizes the main calibration tests performed on the assembled instrument, and their configuration.

3.2. Detune and Cotune Sequences

Characterizing the wavelength dependence of all of the filter elements requires the taking of a great many filtergrams. These filtergrams have to be ordered in special sequences selected for the amount of information they provide. Two kinds of sequences were frequently used: detune and cotune sequences. A detune sequence is a series of filtergrams taken with the Lyot tunable element E1, the NB Michelson, and the WB Michelson out of phase: the tuning phases applied to these elements are such that their peak transmittances do not necessarily coincide. Conversely, a cotune sequence is a sequence in which the three tunable elements are in phase and their peak transmittances coincide. Cotune sequences are used for the normal HMI operations to produce the observables (Doppler velocity, line-of-sight [l.o.s.] magnetic field, full vector magnetic field, and continuum intensity) while detune sequences are used only for calibration purpose. The detune sequence most often applied throughout the HMI calibration phase is a 27-position sequence in which the tuning phases (the 4ϕ of Equation (22))

Table 3. Summary of main ground-test configurations (tests performed on assembled instrument only). OBSMODE is denoted by O, CALMODE by C.

Test	mode	light source	hardware used
wavelength dependence of tunable elements	O/C	dye laser with diffuser	stimulus telescope 24.6-mm field stop in air or vacuum
wavelength dependence of tunable elements	C	heliostat	in air or vacuum
wavelength dependence of non-tunable elements	O/C	dye laser with diffuser	stimulus telescope 24.6-mm field stop wave and power meters in air or vacuum
interference fringes	O/C	lamp	stimulus telescope 24.6-mm field stop
I-ripples total and individual	O/C	lamp	stimulus telescope 24.6-mm field stop
temperature dependence of tunable elements	O/C	dye laser with diffuser	stimulus telescope 24.6-mm field stop in vacuum
thermal stability of tunable elements	O/C	dye laser with diffuser	stimulus telescope 24.6-mm field stop in vacuum
angular dependence of tunable elements	O	dye laser with diffuser	stimulus telescope aperture stop (PCU) 24.6-mm field stop in air or vacuum
angular dependence of tunable elements	C	dye laser with diffuser	stimulus telescope 5-mm field stop in air or vacuum
throughput	C	heliostat	power meter in air or vacuum
tuning polarizer check	O/C	dye laser with diffuser	stimulus telescope 24.6-mm field stop in air or vacuum
artifact check	NA	lamp	stimulus telescope 24.6-mm field stop in air or vacuum

are either 0, 120, or 240 degrees (the total number of variations with repetition of three elements at three positions is 27, hence the length of the sequence). This choice of phases separated by 120° stems from the fact that the sum of the cosines of any set of equally spaced angles is zero, but for a given tunable element, three tuning angles (*i.e.* a separation of 120°) is the minimum number needed to derive the three unknowns (contrast and phase of this tunable element, and integral value of the rest of the transmission profile over the wavelength range).

When the light source emits in a very narrow wavelength range, like the dye laser, this detune sequence allows for an analytical determination of the phases and contrasts of the Michelsons and E1. No fitting procedure is required. This is indeed the only method that we used to determine the contrasts $B(x, y)$ of the tunable elements, at the same time as their phases $\Phi(x, y)$. When using the Sun as the light source, it becomes necessary to fit for the solar Fe I line profile (here conveniently modeled as a Gaussian) concurrently with the phases of the tunable elements. The central wavelength of the solar line is derived from an ephemeris returning the Sun–Earth velocity. With sunlight, it is not possible to obtain the contrasts of the elements, because they are partly degenerate with the ratio of the linedepth over the continuum intensity. Finally, when using the lamp as light source, the detune sequence allows for a characterization (in terms of Fourier coefficients) of the interference fringes produced by the front window and blocking filter.

To check whether or not the tuning polarizer in between the two Michelson interferometers is working properly, we added four positions to the 27-position detune sequence (see Section 4.4). These four positions correspond to four different settings of the HCM of the tuning polarizer.

Close to one thousand detune sequences (with either 27 or 31 positions) have been taken since December 2005.

3.3. Wavelength Dependence Derived From Ground Calibration Tests: Tunable Part of HMI

This is arguably the most important part of the wavelength dependence calibration, because the knowledge of the relative phases of the tunable elements is key to co-tuning HMI and obtaining high-quality data.

3.3.1. Phase and Contrast Maps

Tests with Laser

Using the dye laser as the light source and taking a detune sequence allows the production of phase and contrast maps of the three tunable elements (NB and WB Michelsons, and E1). Figures 5 and 6 show an example of results obtained in CALMODE and OBSMODE.

In OBSMODE, the phase gradient across the tunable elements is less than $\approx 25°$, which is a high degree of spatial uniformity: for the Michelsons, the relative phase ranges are $16°$ and $24°$, while for E1 it is $16°$. The contrasts of the Michelsons and E1 are high (respectively 0.969, 0.996, and 0.962 on average). For comparison, the two Michelson interferometers M1 and M2 in the SOHO/MDI instrument had contrasts that were, on average, 0.92 and 0.98 respectively. Similarly, the range of relative phases for these MDI Michelsons were $17.9°$ and $45.4°$ (for sunlight results). Therefore, taken as a whole, the Michelson interferometers of HMI are more spatially uniform than those of MDI and have better contrasts.

Both OBSMODE and CALMODE sets of maps are very similar, even though the average values are not identical (see Section 3.3.3). A comparison of phase

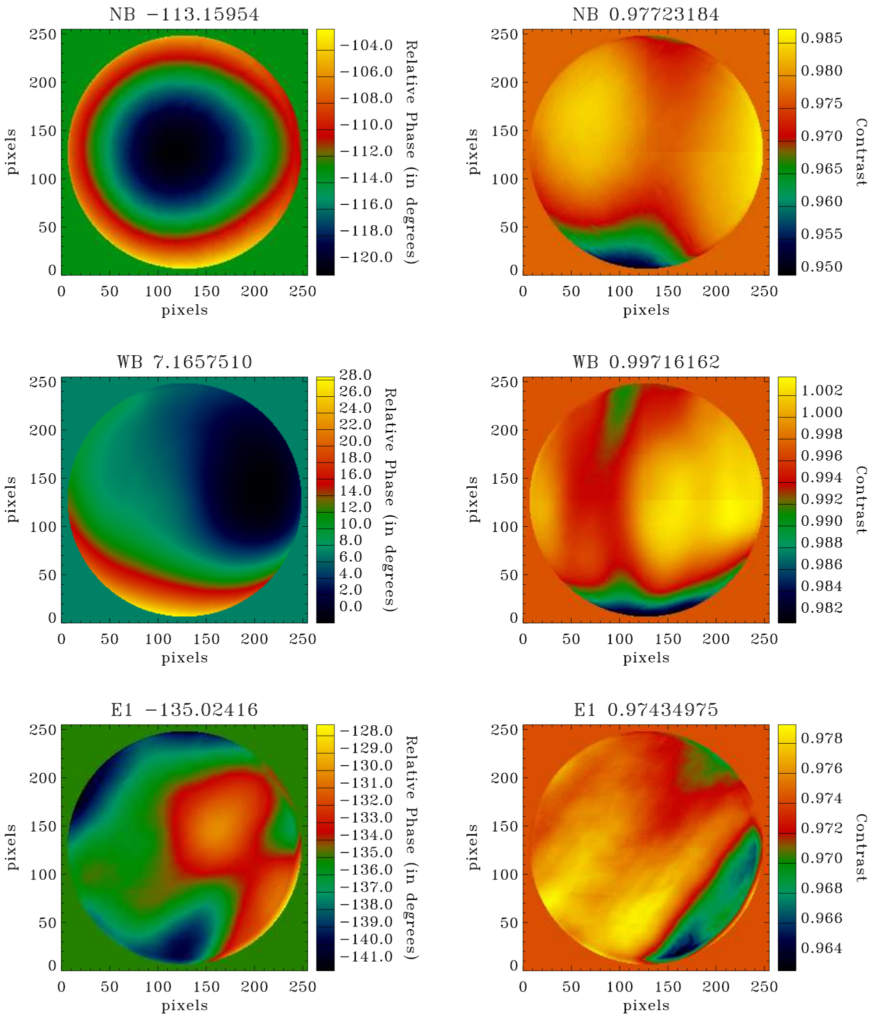

Figure 5. Relative phase (left column) and contrast (right column) maps of the tunable elements obtained in CALMODE with the dye laser as light source in October 2007. The spatially-averaged phases (in degrees) and contrasts are written next to the element name on each panel.

maps obtained from data taken by the front camera with data taken by the side camera shows no systematic difference for the WB Michelson and the Lyot element E1. However, there seems to be a small systematic difference for the NB Michelson (about 0.7° in the sense front camera minus side camera). Detune sequences will be taken during the commissioning phase (the first two months after SDO is launched) to check whether or not this difference is still present. In any case such a difference is not an issue as it does not hamper our ability to properly tune the instrument, and each camera is expected (at least most of the time) to be dedicated to a specific observable category: the one camera to the

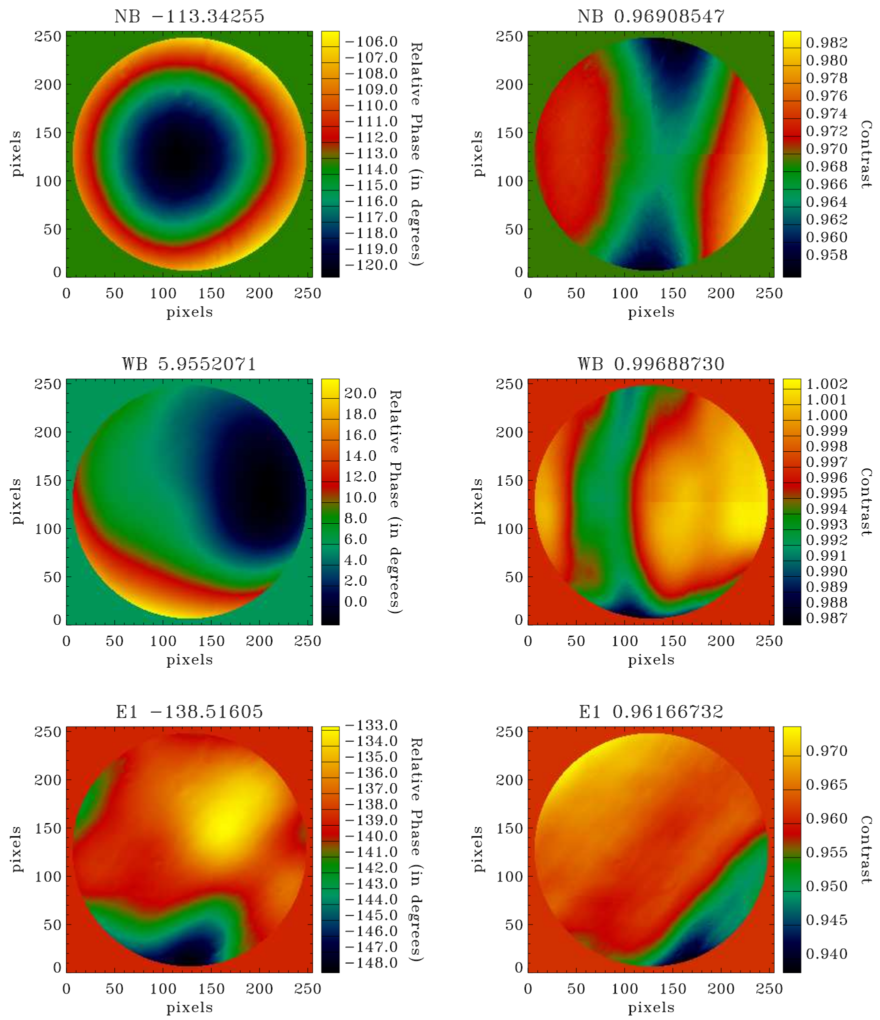

Figure 6. Relative phase (left column) and contrast (right column) maps of the tunable elements obtained in OBSMODE with the dye laser as light source in October 2007. The spatially-averaged phases (in degrees) and contrasts are written next to the element name on each panel.

l.o.s. observables, the other camera to the full vector magnetic field.

Tests with Sun Light

Figure 7 shows phase maps obtained with sunlight data, in CALMODE. The fringe patterns produced by interferences in the front window and blocking filter are clearly visible on the linewidth and linedepth maps. As previously mentioned, no contrast maps can be derived from sunlight data, but the solar continuum intensity, solar line width, and solar line depth are fitted at the same time as

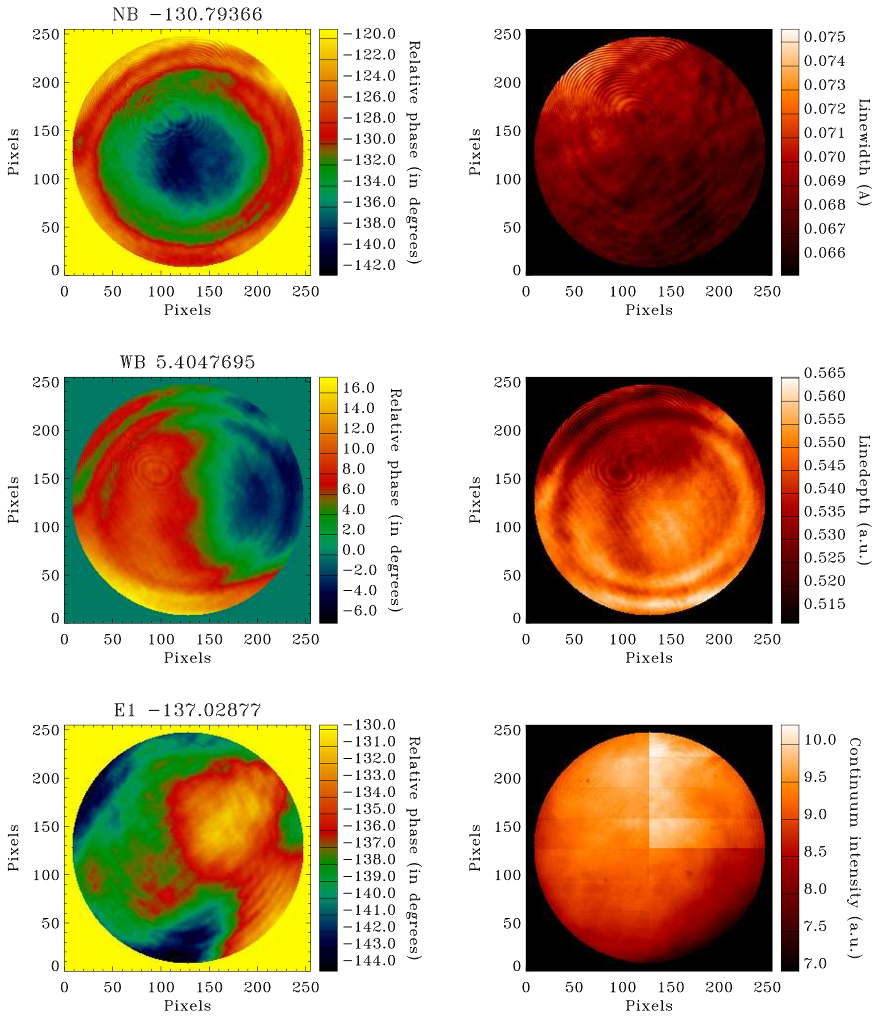

Figure 7. Relative phase, solar-continuum intensity, line-width, and line-depth maps obtained with sunlight through a heliostat, in CALMODE, in September 2007. The spatially-averaged phases (in degrees) are written next to the element name on the panels of the left column.

the relative phases. For the solar line, we need an analytical profile as simple as possible to minimize the number of parameters to fit, and to avoid degeneracies between these parameters. Hence the adoption of a basic Gaussian profile, neglecting any asymmetry present in the actual Fe I line. However, this creates a small systematic error of the phases of the tunable elements, which also translates into a systematic (zero-point) error on the Doppler-velocity determination. This systematic error depends on the velocity at the solar surface and on the position on the solar disk. At disk center, simulations based on a MDI-like algorithm with six sampling positions and averaging the Doppler velocities returned by the first and second Fourier coefficients and by the left and right circular polarizations (see Section 4.5 for details), provide an estimate of the average systematic error of about 80 m s^{-1}, with a change of about 20 m s^{-1} across the velocity range [-6.5,+6.5] km s^{-1} (the sytematic error decreases with increasing velocities).

The non-linear least-squares fit algorithm we apply to fit the relative phases and solar-line parameters is a basic Gauss–Newton algorithm that was extensively tested on artificial data. The relative-phase maps obtained in sunlight and laser light are very similar. In sunlight we only work in CALMODE, because in this mode each location on the front window receives light from the entire — integrated — Sun: therefore, the solar rotation and oscillation velocities cancel out and the solar-line central wavelength is, to a first approximation, only shifted by the Sun–Earth velocity, unlike OBSMODE images for which the value of the solar wavelength is unknown. The solar-limb effect (a redshift of the solar line close to the limb, *e.g.* Dravins, 1982) and the solar convective blueshift (a blueshift of the solar line, especially at disk center, *e.g.* Dravins, 1982) both contribute to the l.o.s. Doppler velocity. Due to the dependence of these effects on the resolution of the instrument, it is difficult to precisely quantify what their impact is on HMI data, especially for ground-based data sensitive to the additional impact of atmospheric seeing. However, neglecting these two effects when calculating the spatially-averaged velocity on the solar disk in CALMODE creates a systematic error (fixed in time) on the relative phases, and therefore a zero-point error on the Doppler velocity maps.

The average phases shown on the figures 5 and 7 are not identical for sunlight and laser light because the laser wavelength is not known accurately (the wavemeter was often off, by as much as a few hundred mÅ), the Fe I solar line is approximated by a Gaussian profile only shifted by the Sun–Earth velocity, and the Michelson interferometer phases drifted in between the detune sequences shown here (taken more than a month apart) as is further explained in the next Section. Finally, any residual differences in the phase maps between sunlight and laser light are likely due to the difference in illumination between these two light sources.

To illustrate the accuracy of our transmittance models of the optical-filter elements, we reconstructed a spatially-averaged detune sequence taken in sunlight and CALMODE. Based on the relative phases, continuum intensity, solar linewidth, and linedepth returned by the fitting code, we calculated at each position of the detune sequence the expected solar intensity (reconstructed intensity). The comparison between reconstructed and original sequences shows that our transmittance models (Equations (12) and (22)) manage to accurately reproduce the data: the maximum relative difference between reconstructed and actual intensities is less than 0.9% and there is no systematic trend in this difference over the sequence.

3.3.2. Drifts of the Phases of the Michelson Interferometers

The relative phases $\Phi(x, y)$ of the Michelson interferometers drift with time. A comparison of these phases obtained during calibration tests in September and October 2007 (both with HMI in the vacuum chamber, with the same oven temperature, and in Sunlight) shows a drift as large as 0.43° a day for the NB

Michelson, and 0.15° a day for the WB Michelson. Other analyses based on dye-laser light returned somewhat smaller drifts (about 0.2° a day for the NB Michelson). In any case, these results warrant regular calibration runs once SDO is launched, to make sure the cotune sequence we use is still optimal.

For comparison, since the launch of SOHO, the phases of the MDI Michelson interferometers have drifted by 218° (for M1) and 43° (for M2) (as of February 2009). The drift rates were much higher immediately after launch than they are now. The tentative explanation for these drifts is that the thickness of the glue holding the mirrors in the Michelsons varies with time, thus changing the optical-path difference.

3.3.3. Phase Difference Between CALMODE and OBSMODE

We observed a systematic difference in the relative phases of the tunable elements obtained in OBSMODE and CALMODE, especially for E1 (the spatially-averaged relative phases differing by about 3° between these two modes) and, to a lesser extent, for the Michelsons. Figure 8 shows these phase differences obtained between two detune sequences taken in laser light in October 2007, for the three tunable elements. The origin of this phase difference is not fully understood. A discrepancy in illumination of the imaged object (whether the front window in CALMODE or a field stop in OBSMODE) and, more significantly, the change in the angle-of-incidence distribution between OBSMODE and CALMODE play a role. A raytrace of HMI obtained with the Zemax software (developed by ZEMAX Development Corporation, www.zemax.com) shows that the rays of light reaching a given point on a HMI CCD are located in a cone during their propagation through the instrument. The diameter of this cone, and, therefore, the distribution of angles of incidence of rays, is different in CALMODE and OBSMODE. For instance, at the quarter-wave plate of E1, the Zemax model shows that the maximum angle of incidence of sunrays is 0.9737° in CALMODE, while it is 1.0270° in OBSMODE (with the first focus block). Since the angular dependence of the tunable elements is non-zero, this small difference between angles of incidence in OBSMODE and CALMODE impacts the relative phases (see Section 3.7).

Simulations show that the observed phase difference introduces an almost-constant (peak-to-peak variation of 5 m s^{-1}) systematic error in the solar oscillation Doppler velocity determination (zero-point error) because this Doppler velocity is computed based on phase maps obtained in CALMODE, while the observations are performed in OBSMODE. Indeed, by applying the MDI-like algorithm with six sampling positions and averaging the Doppler velocities returned by the first and second Fourier coefficients and by the left and right circular polarizations (see Section 4.5 for details), we estimate that this sytematic error varies between ≈ 26 and ≈ 31 m/s in the velocity range $[-6.5, +6.5]$ km s^{-1}. The impact on the rms variation (produced by photon noise) of this Doppler velocity is hardly noticeable across the velocity range.

3.3.4. Free Spectral Range Calibration

The FSRs of the Lyot elements and Michelson interferometers were measured using spectrographs and collimated light, before HMI was assembled. It is pos-

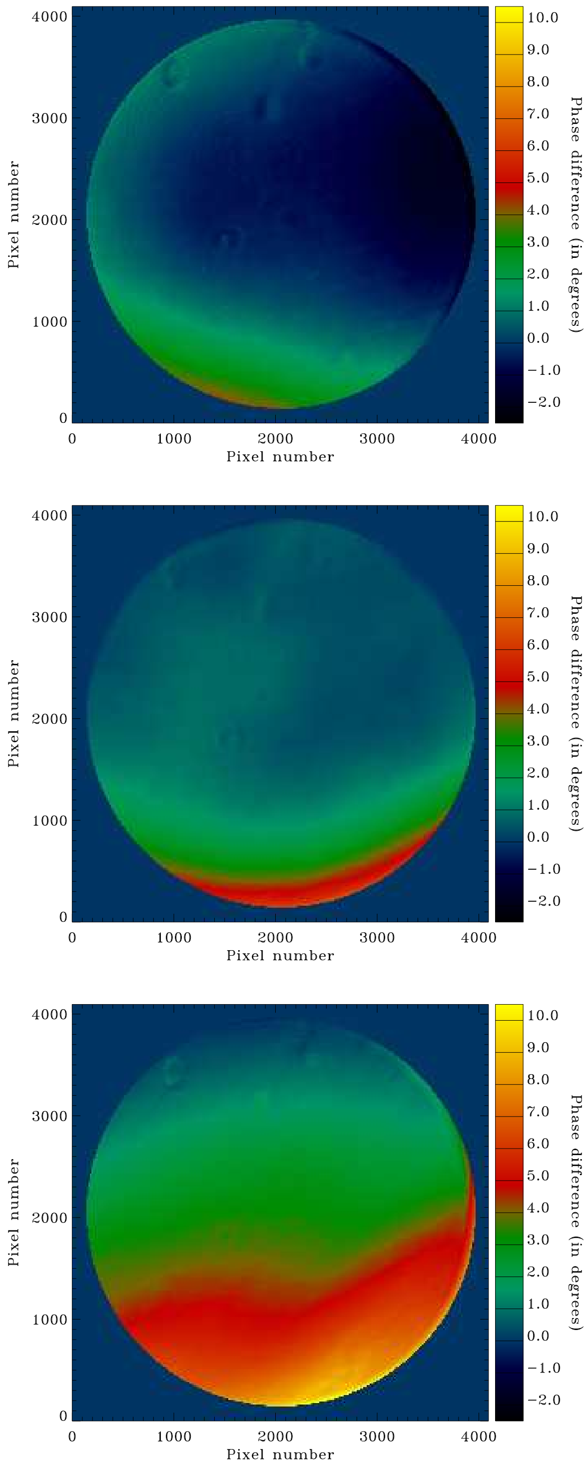

Figure 8. Relative-phase difference CALMODE minus OBSMODE for two detune sequences taken in vacuum and with laser light in October 2007. Upper panel: NB Michelson; middle panel: WB Michelson; lower panel: Lyot element E1.

Table 4. Full Spectral Ranges of the Michelson interferometers and Lyot elements. FSR_n are the nominal FSRs, and FSR_m are the measured ones (measured by the manufacturer for the Michelson interferometers, and individually measured at LMSAL for the Lyot elements), in mÅ at 6173 Å.

Element	FSR_n	FSR_m
NB	172	172
WB	344	343.1
E1	690	693
E2	1380	1407
E3	2758	2779
E4	5516	5682
E5	11032	11354

sible to determine the FSRs of the tunable elements for the proper distribution of incidence angles with a greater precision, for instance by taking two detune sequences at different dye-laser wavelengths. From these two sequences, two sets of relative phases [Φ] of the tunable elements are derived. Any difference in the phases results from an error on the FSRs. We applied this method, taking many detune sequences at various dye-laser wavelengths and averaging the resulting FSRs. However, it proved difficult to obtain an accurate measurement of these FSRs on the ground, because, among other issues, the dye-laser wavelengths were not always stable. The laser intensity was fluctuating, and there was a generally high level of noise. We derived the following, possibly underestimated, estimates of the FSRs: 0.1709 Å for the NB Michelson (instead of the nominal 0.1720 Å), 0.3419 Å for the WB Michelson (instead of 0.3440 Å), and 0.6935 Å for E1 (instead of 0.6900 Å). These values are well within the specifications. Measurements of these FSRs at LMSAL while the Michelsons and E1 were outside of the instrument — and therefore for a different distribution of angles of incidence — returned: 0.1724 Å for the NB Michelson and 0.6930 Å for E1. The FSR of the WB Michelson was not measured at LMSAL, but reports from the manufacturer, LightMachinery, give an estimate of 0.3431 Å (and, for information, the same manufacturer reports 0.172 Å for the FSR of the NB Michelson). The FSRs of the non-tunable elements (E2 to E5) were measured at LMSAL while they were outside of the instrument, and are shown in Table 4.

After launch, we plan to use the orbital velocity of SDO to determine the FSRs of the tunable elements with a better accuracy than was obtained from the ground. For instance, a 1 m/s accuracy on the Sun-SDO radial velocity translates into an accuracy of 0.02 mÅ on the solar line central wavelength, far better than the accuracy on the dye laser wavelength (of the order of 10 mÅ).

3.4. Wavelength Dependence Derived From Ground Calibration Tests: Non-Tunable Part of HMI

Taking detune sequences at different dye-laser wavelengths spanning a wide enough wavelength range allows a determination of the relative phase and con-

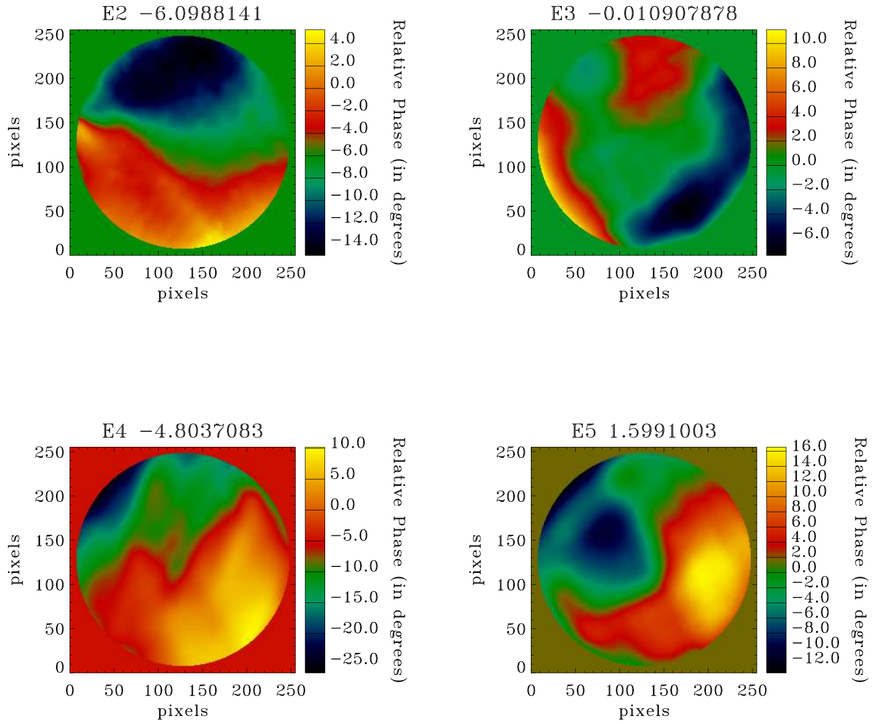

Figure 9. Relative phases of the non-tunable elements. Dataset of 15 October 2007. OBSMODE images. The blocking filter center is at ≈ -1 Å from target wavelength. The average phases (in degrees) are written next to the element name on each panel.

trast maps of the non-tunable elements. Examples of such maps are shown on Figures 9, 10, 11, and 12, in OBSMODE and CALMODE. They were obtained from detune sequences taken in vacuum at 30 different laser wavelengths in October 2007, ranging from 6167.5 to 6179.0 Å.

The determination of these phase and contrast maps is difficult because the intensity levels on the CCDs drop quickly for wavelengths far from the target one. These wavelengths are needed for an accurate computation of the characteristics of the elements with the largest FWHMs (E4 and E5). Moreover, the FWHM of E5 (about 5.7 Å) is relatively close to the one of the blocking filter (about 8 Å), which complicates the determination of its phases and contrasts. Thus the center of the blocking filter transmission profile needs to be known to avoid a degeneracy with the peak transmittance of the profile of E5 (and, to a lesser extent, E4). To estimate the center location, we used three transmission profiles of the blocking filter provided by the Andover Corporation at three different temperatures and two angles of incidence. We assumed a quadratic dependence on temperature of the blocking filter wavelength shift [$\delta\lambda$], and an angular de-

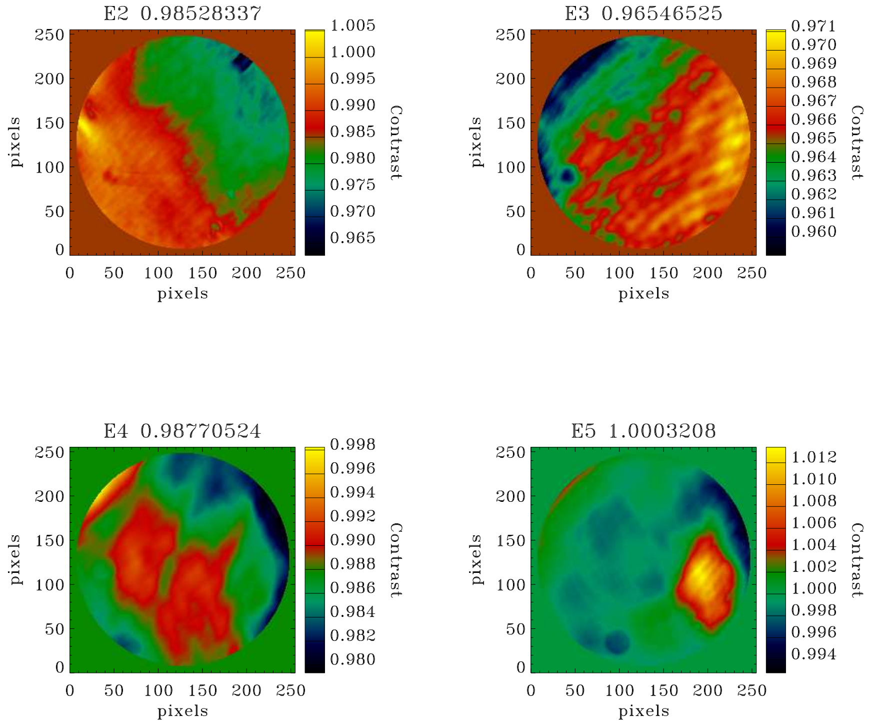

Figure 10. Contrasts of the non-tunable elements. Dataset of 15 October 2007. OBSMODE images. The blocking filter center is at ≈ -1 Å from target wavelength. The average contrasts are written next to the element name on each panel.

pendence following Equation (30). An uncertainty of a few hundred mÅ on the center of the blocking filter is not an issue as the fitting code computing the phases and contrasts compensates by shifting the average phase of E5 (and to a lesser extent E4) so that the goodness of fit and the non-tunable transmission profile remain essentially unchanged. For a proper fitting, the laser wavelengths and the fluctuations in laser intensity need to be accurately known. The fitting procedure, a Gauss–Newton algorithm, favors the high intensities obtained with wavelengths close to the target one. This results in a poor determination of the contrasts. To improve this determination, we added a weighting scheme to our code. The weights [W] are set to $W = 1/\sqrt{1+KI}$ where $K = 256$ and I is the intensity (I is the value in DNs from the filtergram, normalized by a factor 10 000 and corrected to account for changes in the laser intensity and exposure time between the different detune sequences): we multiply the data intensities by these factors. The weights were chosen to better represent the actual errors of the intensities, which have photon, gain, and constant noise. Several values of K were tested before selecting $K = 256$. This is the lowest value for which

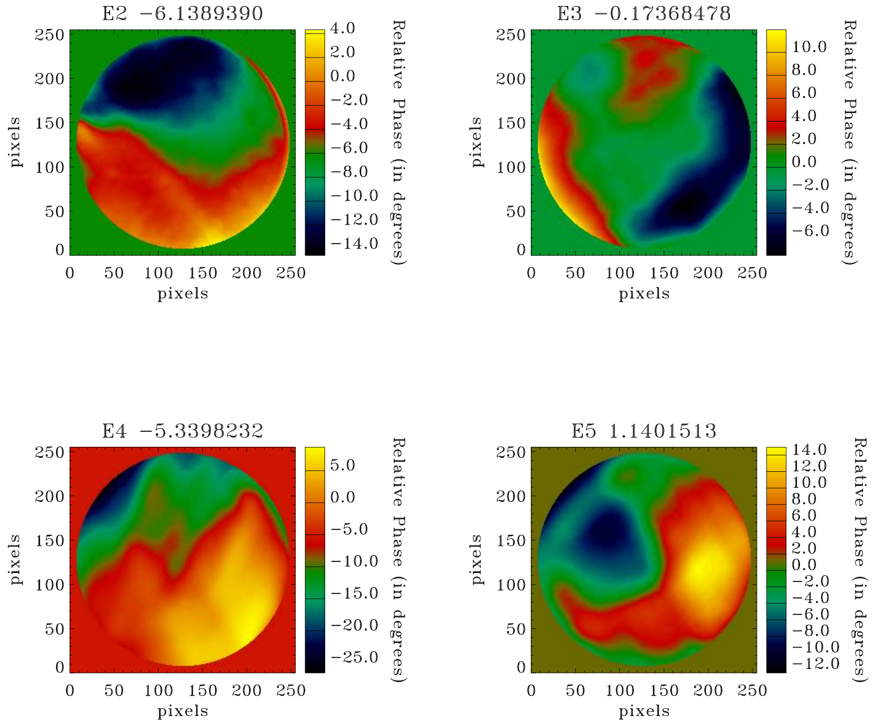

Figure 11. Relative phases of the non-tunable elements. Dataset of 15 October 2007. CALMODE images. The blocking filter center is at ≈ -1 Å from target wavelength. The average phases (in degrees) are written next to the element name on each panel.

the spatially-averaged contrasts on the non-tunable elements are lower than, or equal to, 1 (instead of average values as high as 1.2). However, locally some fitted contrasts are still unrealistically larger than one.

The results of Figures 9, 10, 11, and 12, show that the non-tunable elements have a good degree of spatial uniformity in terms of phases $\Phi(x, y)$: the range is $\approx 19°$ for E2, $\approx 20°$ for E3, $\approx 36°$ for E4, and $\approx 30°$ for E5. These elements also have high contrasts (on average, larger than 0.96). The phase maps are very similar in OBSMODE and CALMODE. Other measurements of the phase maps of the non-tunable elements were performed at LMSAL in October 2005 while these elements were outside of the instruments. These data were obtained in a collimated light beam for which all of the rays are normal ($\theta = 0$). Despite this difference, the same features are visible on both sets of maps, and they display relatively similar phase gradients after we convolve the LMSAL maps with a mask to simulate the impact of the proper light distribution at an image point (except for the element E2 for which there are some noticeable differences).

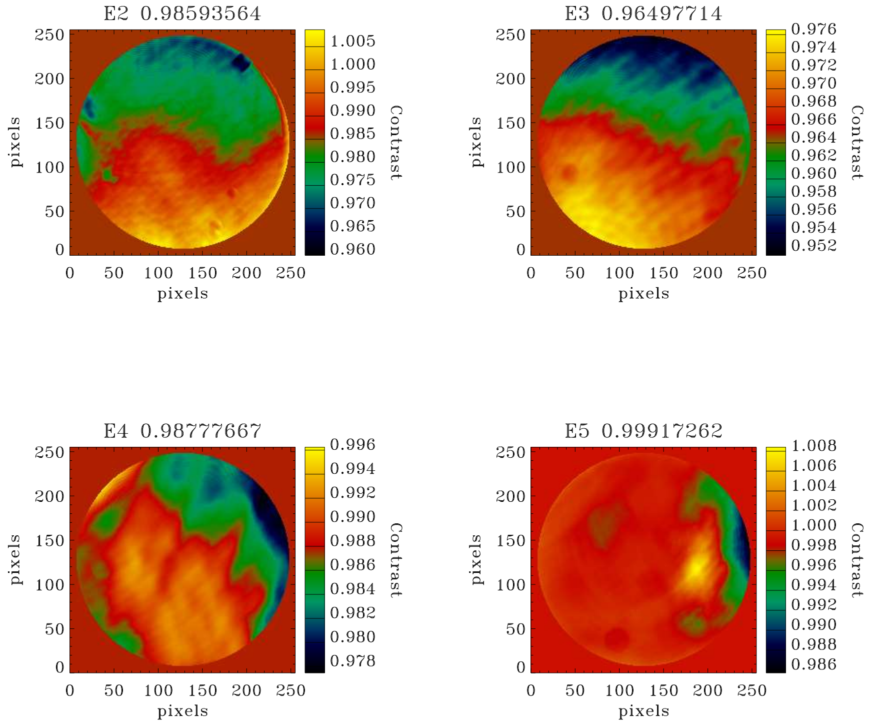

Figure 12. Contrasts of the non-tunable elements. Dataset of 15 October 2007. CALMODE images. The blocking filter center is at ≈ -1 Å from target wavelength. The average contrasts are written next to the element name on each panel.

The spatially-averaged transmission profile of the non-tunable part of HMI is shown on Figure 13 (black line). This profile can be compared to measurements obtained in October 2006 with lamp light and a spectrograph (red line). During these measurements performed at LMSAL, the blocking filter was absent, the lamp had a background infra-red intensity that contaminated the transmission profiles, and the actual profile was convolved by the resolution window of the spectrograph. E1 was tuned at 36 different positions with a polarizer. Because the light from the lamp was also slightly polarized, the resulting non-tunable transmission profile (obtained by averaging the 36 profiles) is contaminated by the E1 profile. Despite all these differences, both transmission profiles look rather similar (note that we shifted the red curve in wavelength so that it overlaps the black one). The maximum transmittance is located at about +16 mÅ from the target wavelength, and the FWHM of the non-tunable profile is 624.5 mÅ (slightly larger than the nominal value of 612 mÅ).

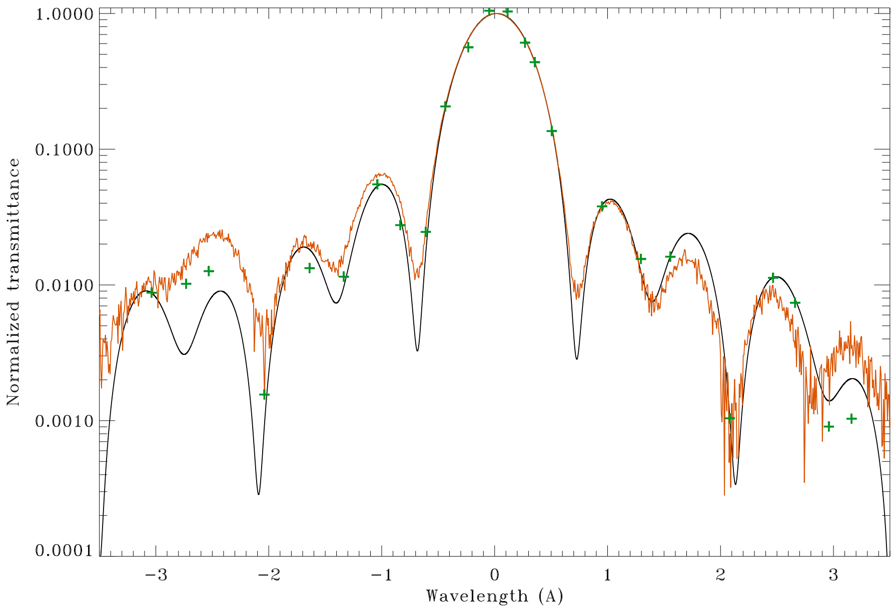

Figure 13. Spatially-averaged transmission profiles of the non-tunable part of the HMI filter. Black line: model obtained by fitting for the phases and contrasts of the non-tunable elements, using detune sequences in laser light and CALMODE taken at different laser wavelengths in October 2007; green crosses: datapoints (each point is an average of the 27 intensities of the corresponding detune sequence); red line: measurements obtained with lamp light and a spectrograph while the Lyot filter was outside the instrument (the blocking filter was absent).

3.5. Interference Fringes Produced by the Front Window and Blocking Filter

The use of the lamp as light source while taking detune sequences allows a characterization of the fringe patterns produced by the front window and blocking filter. In CALMODE, the front window is in focus, unlike the blocking filter. In OBSMODE, both the front window and blocking filter are out of focus. Therefore a comparison between the results of CALMODE and OBSMODE detune sequences emphasizes the fringes produced by the front window only. Our fitting code expands the non-tunable transmission profile of HMI in the limited range $[-2\,\mathrm{FSR}_{\mathrm{NB}}, +2\,\mathrm{FSR}_{\mathrm{NB}}]$ (where $\mathrm{FSR}_{\mathrm{NB}}$ is the FSR of the NB Michelson) into a Fourier series, and fits for the first seven Fourier coefficients, on top of the mean value (zero frequency).

Indeed, at any position of a detune sequence, the intensity on the CCD is equal to the wavelength-independent lamp intensity times the integral value (over the wavelength) of the transmittance of the non-tunable part of HMI multiplied by the three transmittances of the tunable elements. Here these three transmittances are modeled following Equation (22). Applying trigonometric identities to separate the terms in $2\pi\lambda/\mathrm{FSR}$ from the terms in $\Phi+\phi$ (the tuning positions), and assuming that the FSR of the WB Michelson is twice the FSR of NB and the FSR of E1 is four times the FSR of NB (which is close to the actual values), we obtain an expression in which the total transmittance is expressed in terms of cosines and sines of $2\pi\lambda K/(4\,\mathrm{FSR_{NB}})$ where K ranges from 0 to 7, and in terms of tuning positions. Therefore, the transmittance of HMI at each detune position can be expressed as a combination of 14 Fourier coefficients (7 cosines and 7 sines) of the non-tunable transmission profile (in the range $[-2\,\mathrm{FSR_{NB}}, +2\,\mathrm{FSR_{NB}}]$), and of constants depending on the tuning positions. Since these constants can be calculated and the intensities on the CCD at each tuning position can be measured, it is theoretically possible to derive the seven Fourier coefficients of the non-tunable transmission profile, plus its mean value. The corresponding seven spatial frequencies f range from $1/(4\,\mathrm{FSR_{NB}}) \approx 1.462$ Å^{-1} to $7/(4\,\mathrm{FSR_{NB}}) \approx 10.234$ Å^{-1}. Figures 14 and 15 show the fringe patterns at some selected spatial frequencies expressed in terms of $\mathrm{FSR_{NB}}$, in OBSMODE and CALMODE. On these figures, the amplitude of the Fourier coefficients is very low for $f = 3/(4\,\mathrm{FSR_{NB}})$.

Because the interference fringe patterns are connected to different glass block thicknesses (see, *e.g.*, Equation (31)), we can theoretically deduce where the interferences occur in the front window and/or blocking filter. It is easier with the front window, composed of glass blocks of thicknesses 6, 3, and 6 mm. Partial reflections at the interfaces of these blocks can create fringes with the spatial frequencies $f = 1/\mathrm{FSR}$, with FSR expressed by Equation (31). The refractive index of the glass blocks is $n = 1.516$ at the target wavelength λ. The three thicknesses $[d]$ for which significant fringe patterns are observed (assuming normal rays) are 3, 6, and 9 mm (the respective spatial frequencies being $f = 2.39$, 4.77, and 7.16 Å^{-1}). Figure 16 shows the cosine and sine transform coefficients at these specific frequencies.

Both the front window and the blocking filter produce fringes. The main issue is that these fringes move with temperature, as was confirmed by thermal tests in which the front window temperature, and (not at the same time) the oven temperature, were changed. The overall amplitude of the interference patterns does not seem to be affected by these temperature changes, but the phases of the patterns are. This will be a problem after the regular eclipses affecting SDO, or any event changing the temperature gradient and/or temperature average on the front window.

3.6. *I*-ripple

As mentioned in section 2.4, even with a perfect HMI optical filter the output intensity is expected to vary slightly from a filtergram sequence position to another. The resulting *I*-ripple is estimated at a few tenths of a percent, by calculating the theoretical intensities resulting from perfect transmittances of the different HMI elements (*e.g.*, phases equal to zero, contrasts equal to one for the Lyot elements and the Michelsons, and Gaussian profile centered at the target wavelength for the blocking filter), for all the 27 positions of a detune sequence. In July 2006, a significant *I*-ripple ($> 10\%$) was detected with detune sequences in white light. The root causes were misalignements in the Lyot element E1. This element was de-assembled, re-aligned, and then re-assembled. The overall *I*-ripple we derive from detune sequences, taken after re-assembly of the Lyot filter,

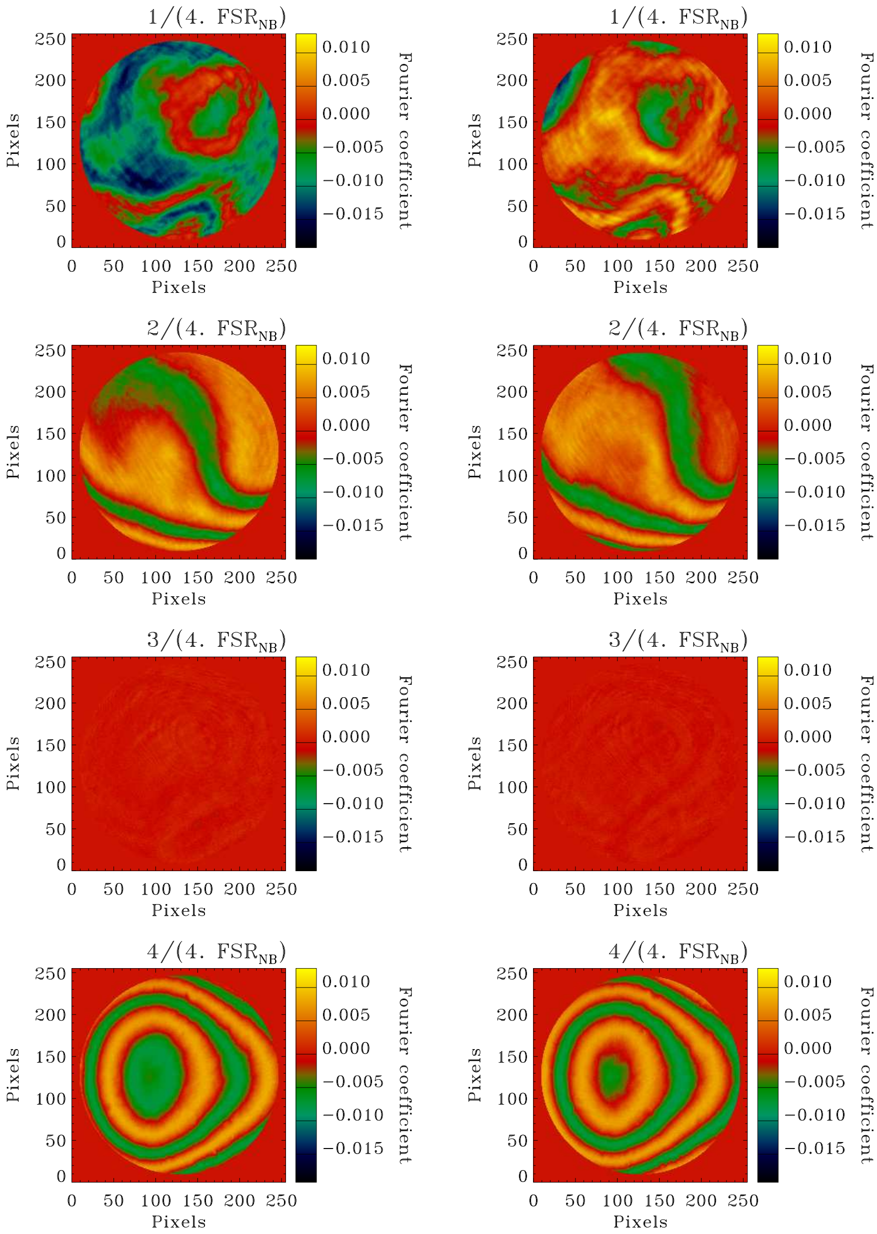

Figure 14. Fourier coefficients of the expansion of the transmission profile of the non-tunable part of HMI into a Fourier series, at a few selected spatial frequencies. Left panels: Fourier coefficients for the cosines; right panels: Fourier coefficients for the sines. The title of each panel is the spatial frequency (in terms of the FSR of the NB Michelson) corresponding to the coefficient. September 2007 data obtained in vacuum and OBSMODE.

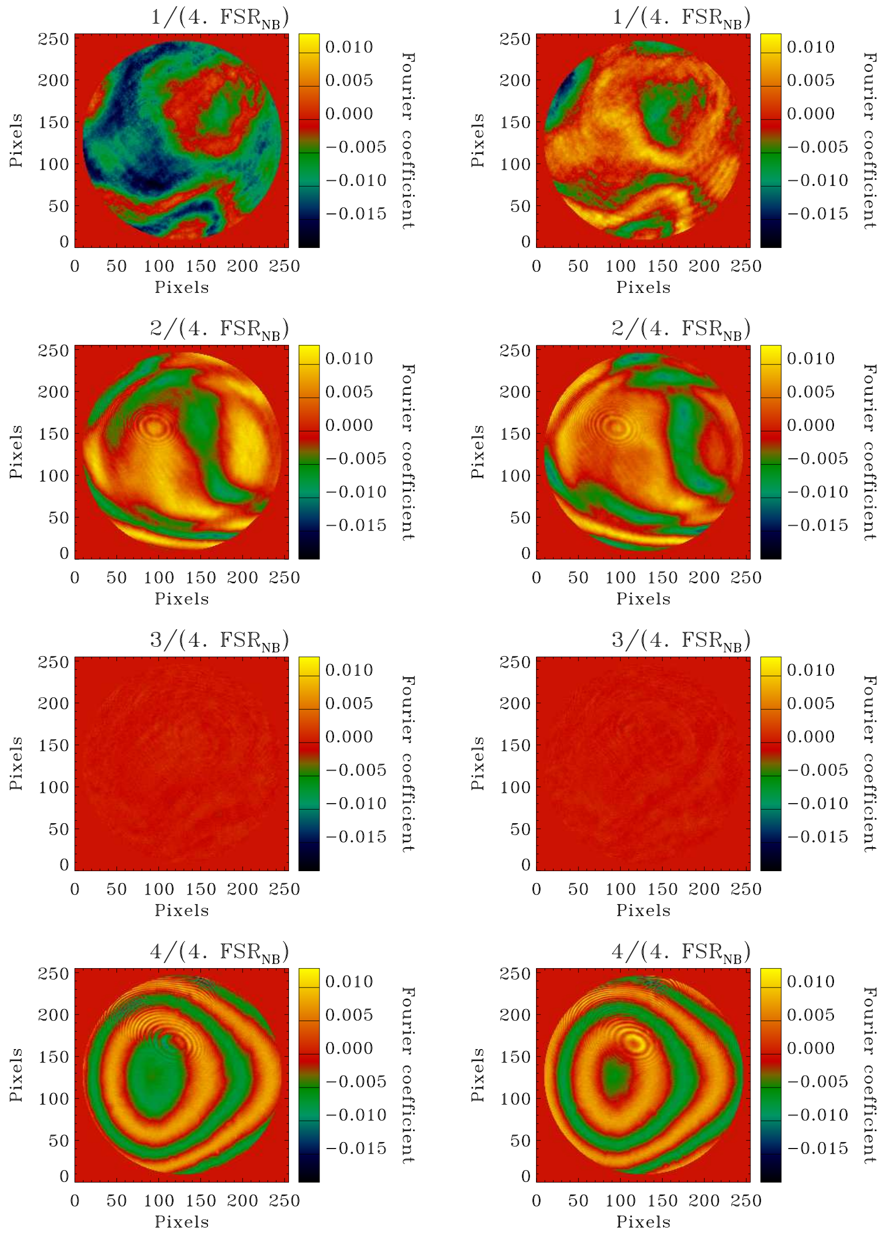

Figure 15. Fourier coefficients of the expansion of the transmission profile of the non-tunable part of HMI into a Fourier series, at a few selected spatial frequencies. Left panels: Fourier coefficients for the cosines; right panels: Fourier coefficients for the sines. The title of each panel is the spatial frequency (in terms of the FSR of the WB Michelson) corresponding to the coefficient. September 2007 data obtained in vacuum and CALMODE.

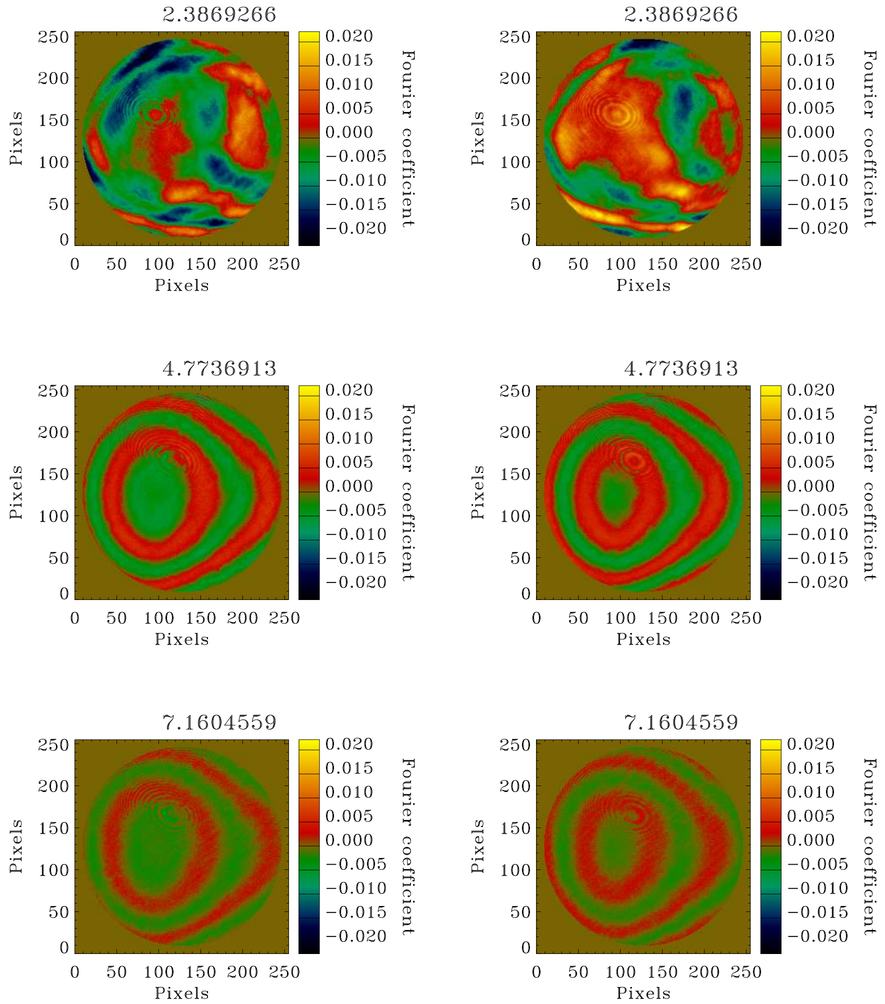

Figure 16. Cosine and sine coefficients of the transmission profile of the non-tunable part of HMI, at spatial frequencies corresponding to the front window components. Left panels: cosine coefficients; right panels: sine coefficients. The title of each panel is the spatial frequency corresponding to the coefficient (in Å^{-1}). September 2007 data obtained in vacuum and CALMODE.

in OBSMODE and CALMODE, is of the order of 1.9%, much lower than the previous I-ripple but still higher than what is expected for a perfect instrument. Figure 17 shows an example of I-ripple measurement obtained in vacuum in September 2007, on spatially averaged intensities of two detune sequences.

If we adopt Equation (33) as a model of the HMI individual I-ripples, the values of K_0, K_1, and K_2 can be fitted for each tunable element separately using a fine-tuning sequence taken in white light. A fine tuning sequence is a sequence of filtergrams in which one tuning HCM is rotated all the way by a

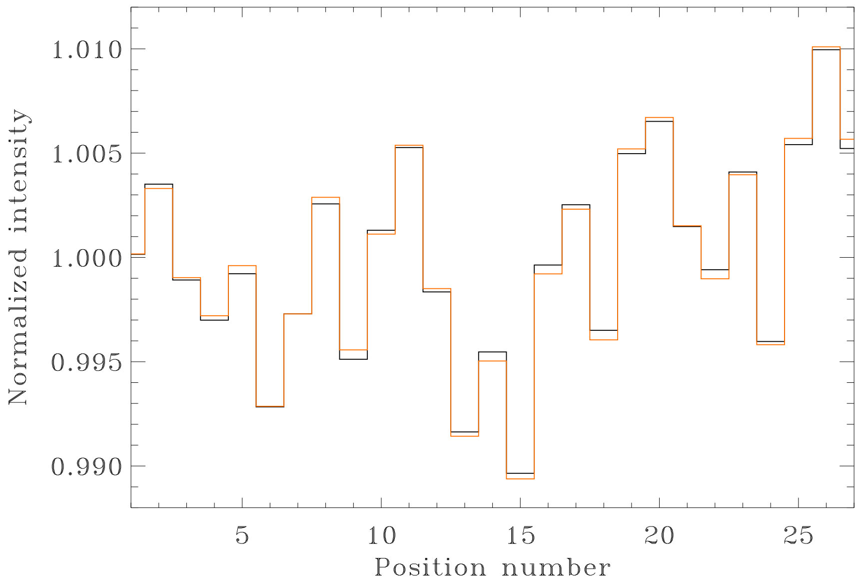

Figure 17. Variation of the spatially-averaged intensity measured on the HMI CCDs during detune sequences in white light. Black curve: OBSMODE detune sequence; red curve: CALMODE detune sequence. Data of September 2007, taken in vacuum. No field stop was used for the OBSMODE sequence, while the 24.6 mm stop was used for the CALMODE sequence.

given number of steps while the other tuning HCMs are fixed. Such a sequence was taken in October 2006 after re-assembly of the Lyot filter, and returned the following estimates for the individual I-ripples: 2.03% for E1, 1.15% for the NB Michelson, and 0.99% for the WB Michelson. Figure 18 shows these individual I-ripples. In August 2009, other fine tuning sequences were taken which returned somewhat smaller I-ripples: 0.98% for E1, 0.81% for NB, 0.78% for WB, and an overall I-ripple of 1.87%. A better (less flickering) light bulb could account for part of this difference.

With the simple models of transmittance for the Lyot elements and the Michelsons used in this article (Equations (12) and (22)), the impact of an I-ripple is neglected. Simulations show that, in the case of a misaligned half-wave plate in E1, this neglect produces a zero-point error (systematic error) on the determination of the Doppler velocity of, at most, several tens of m s^{-1}. This systematic error varies almost linearly across the range $[-6.5, +6.5]$ km/s. Therefore, it is theoretically possible to correct most of it by using the orbital velocity of SDO once the satellite is launched. Moreover, not taking into account the I-ripple in this case does not seem to have any impact on the rms variation of the solar Doppler velocity resulting from photon noise.

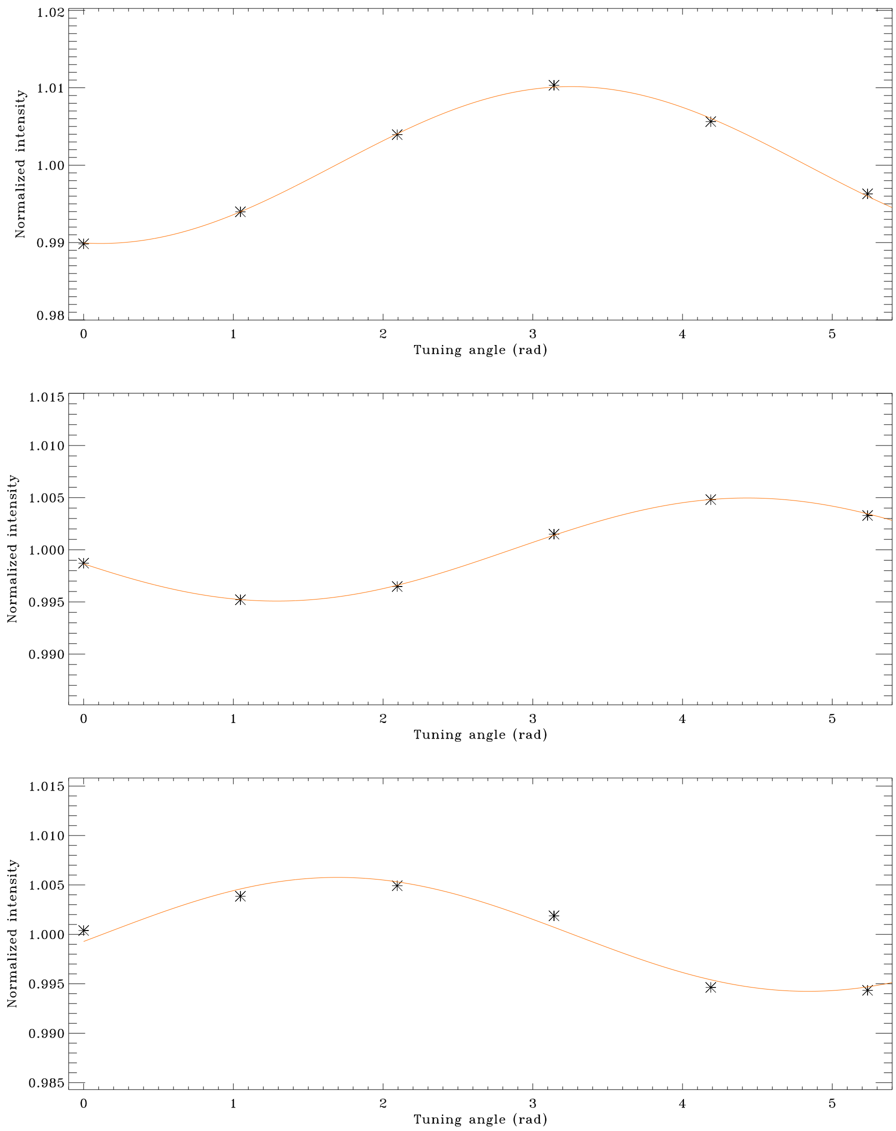

Figure 18. Variation of the spatially-averaged intensity measured on the HMI CCDs during a fine-tuning sequence in white light in October 2006. Black stars: data points; red curves: fit by Equation (33). Upper panel: Lyot element E1; middle panel: WB Michelson; lower panel: NB Michelson.

3.7. Angular Dependence

Angular dependence tests were performed with the dye laser as light source. The setup is different in OBSMODE and CALMODE. In OBSMODE, an opaque mask with a circular hole (about 25 mm in diameter) mounted on the Polarization Calibration Unit (PCU) is placed in between the stimulus telescope and the front window (aperture stop), and the 24.6 mm field stop is used. Depending on the position of the hole (its radial distance from the center of the HMI aperture and its polar angle on the plane of this aperture), specific incidence and azimuthal angles are selected. In CALMODE, the 5-mm field stop is placed at the focal plane of the stimulus telescope. Detune sequences were taken at nine different hole/field stop locations, and the corresponding phase maps of the tunable elements were derived.

The main issue with these setups is that a change in incidence and azimuthal angles is intertwined with a change in the path of the rays of light inside the instrument; therefore, spatial and angular dependences are entangled. Using ray traces of the instrument modeled with the Zemax software, we access the theoretical image sizes in OBSMODE and CALMODE at different locations in HMI, and also the diameters of the light cones (rays of an image point are distributed in a cone-shaped beam inside HMI). These data are needed to determine how to shift the resulting phase maps to cancel out the spatial-dependence effect. The value of the selected incidence angle at each tunable element can also be obtained from the Zemax software. Angular dependence tests were performed in March 2006 (in air) and February 2007 (in vacuum). The results of these tests were challenging to analyze, and at times confusing, due to the spatial and angular dependence entanglement and to changes in the laser wavelength in-between detune sequences. These results seem to show a weak angular and azimuthal dependence for the Michelsons. E1 seems to be the tunable element with the strongest angular dependence, followed by the NB Michelson, and the WB Michelson. This is hardly surprising as the retardance of the Michelson interferometers is expected to vary mainly as θ^4 (for small θ) if the WF compensation is perfectly achieved, while the retardance of E1 is expected to vary as θ^2 (see Sections 2.1 and 2.2). Moreover, there seems to be a significant amount of azimuthal dependence with E1, which implies that some elements of the WF components are not perfectly aligned (either the split crystals or, more likely, the half-wave plate). Such a misalignment could explain the existence of the observed I-ripple (based on Equation (33), a tilt by $2°$ of the half-wave plate creates a $\approx 1.25\%$ I-ripple for E1).

Figure 19 shows the wavelength change [$\delta\lambda$] produced by a non-zero incidence angle [θ]. We fit the data points by a second-order polynomial [$\delta\lambda = a\theta^2 + c$] where a and c are the two polynomial coefficients (there is no term in θ because we assume symmetry around the axis $\theta = 0$). We present two cases for the tunable element E1: one for the azimuthal angle (among those measured) where the angular dependence is the strongest (corresponding, on the coordinate system of a HMI filtergram and counting the angles positively counterclockwise from the horizontal axis to the right, to the hole being centered at $-90°$), and one for which it is the weakest (corresponding to the hole centered at $+90°$).

The maximum wavelength change measured is at $\theta \approx 0.9^\circ$ (close to the edge of the field of view) and is $\delta\lambda \approx 51$ mÅ (the minimum change at $\theta \approx 0.9^\circ$ appears to be only ≈ 5.5 mÅ). For the NB Michelson, the maximum wavelength change measured is much less, $\delta\lambda \approx 14$ mÅ, and for the WB Michelson it is only $\delta\lambda \approx 8.5$ mÅ.

Another way of observing the angular dependence in CALMODE at the center of the aperture of the tunable elements is to compare their phase maps obtained through a detune sequence taken with the solar-size field stop to phase maps obtained with the small field stop (centered). Raytraces in CALMODE show that the maximum angle of incidence in the light beams inside the instrument varies, at the center of E1, from 0.17° (with the small field stop) to 0.96° (with the solar-size field stop). Therefore, any phase difference derived from these two detune sequences results mostly from the change in the distribution of the angles of incidence. This test confirms that E1 has a stronger angular dependence than the Michelsons. For instance, the results of two detune sequences taken three days apart with the different field stops and in similar conditions (same laser wavelength, same oven temperature, and in vacuum), in February 2007, show an average phase shift of 14.3° for E1, corresponding to a 27.5 mÅ wavelength change. This change, when extrapolated to $\theta = 0.9^\circ$, is about 70 mÅ, larger than the maximum 51 mÅ change previously reported.

This relatively strong angular dependence partly explains the $\approx 3^\circ$ averaged phase difference for E1 between CALMODE and OBSMODE. It is difficult to quantify the contribution of the angular dependence to this phase difference, but by using the angles of incidence in OBSMODE and CALMODE returned by the Zemax software for E1, and applying the strongest dependence displayed on Figure 19, it seems that, at most, $\approx 1.5^\circ$ can be explained by the angular dependence. The Michelsons show a smaller phase difference between OBSMODE and CALMODE: this seems consistent with their weaker dependence on θ.

3.8. Temperature Dependence

During calibration runs in vacuum, the oven temperature was changed from 28 to 35°C. Taking detune sequences with the dye laser at three different stable oven temperatures, allows the derivation of the temperature dependence of E1 and the Michelsons. Figure 20 shows some results. We fit the three temperature points with a second-order polynomial because the temperature dependence is theoretically quadratic (see for instance Equation (15)). The slope is the lowest around $31-31.5$°C. At 30°C, the nominal oven temperature, the slopes are -9.5 mÅ $^\circ$C^{-1} for the NB Michelson, -9.7 mÅ $^\circ$C^{-1} for the WB Michelson, and -12.4 mÅ $^\circ$C^{-1} for the Lyot element E1. This is a relatively weak temperature dependence and is therefore fully satisfactory. In terms of relative phases, Φ increases with the oven temperature for temperatures below ≈ 31.5°C, and then decreases.

The temperature dependence of the Lyot elements was also investigated at the LMSAL facility in October 2006 while the Lyot filter was outside of the instrument, using sunlight and a spectrograph. Fits of the transmission profiles returned by this spectrograph at different temperatures show that the Lyot

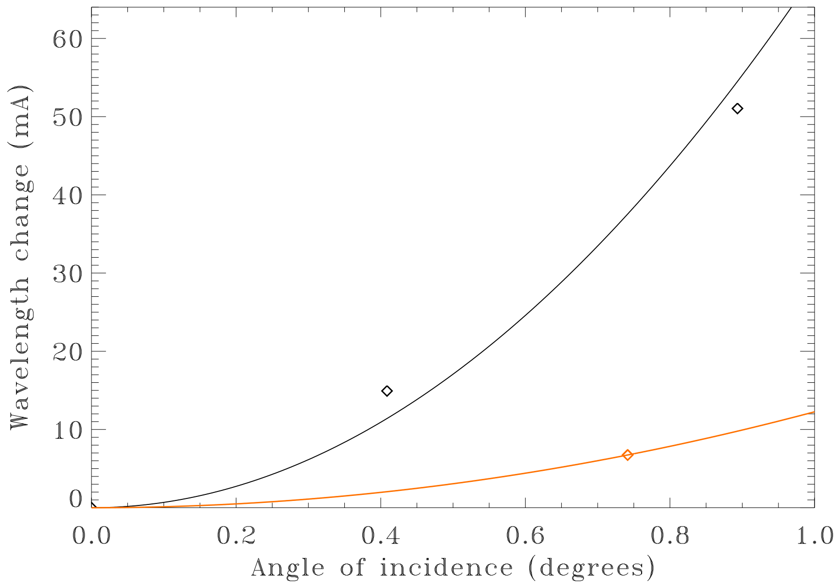

Figure 19. Angular dependence of the tunable element E1 in CALMODE. The diamonds show the data points, and the solid lines are the results of second-order polynomial fits (we assumed the data are symmetrical around $\theta = 0$). We show the results for the azimuthal angle, amongst those measured, corresponding to the maximum angular dependence (black line), and for the one corresponding to the minimum angular dependence (red line).

elements are thermally well compensated: the absolute value of the slope around 30°C is less than $\approx$ 10 mÅ°C^{-1} (see Table 2). In particular, for E1, the data from October 2006 show a decrease in the wavelength of peak transmittance from 25 to $\approx 31 - 32$°C, and then an increase, in agreement with the results presented here.

Finally, we also checked the dependence of the *I*-ripple on the oven and front-window temperatures, using lamp-light detune sequences taken at different stable oven temperatures or stable front-window temperatures. This confirmed that the *I*-ripple is largely independent of any oven temperature change within the range 28 to 35°C, and is similarly largely independent of any front-window temperature change within the range 20 to 30°C.

4. Other Calibration Results

4.1. Thermal Stability of the Tunable Elements

The phases of the tunable elements exhibit a temperature dependence, as detailed in the previous section. However, this temperature dependence was obtained for stable oven temperatures: the temperatures were constant during a detune sequence, and *a priori* uniform across the tunable element apertures.

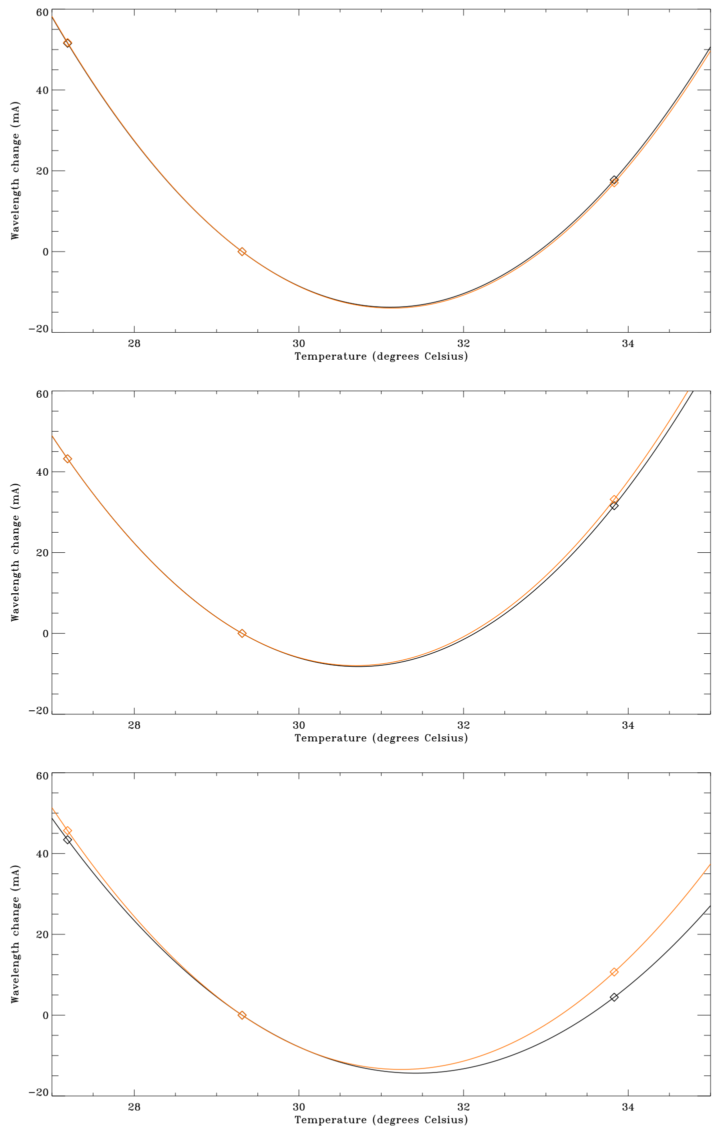

Figure 20. Temperature dependence of the tunable elements. Upper panel is for the NB Michelson, middle panel is for the WB Michelson, and lower panel is for the Lyot element E1. The diamonds show the data points, while the solid lines are second-order polynomial fits. The black lines are for OBSMODE data, the red lines are for CALMODE data. The zero-wavelength change was arbitrarily assigned to the $T_e \approx 29.5°$C point.

A change in the oven temperature propagates in a finite time to the different tunable elements, and most likely creates a temperature gradient across their aperture. Therefore, here, we are interested in answering the questions: how do the tunable-element phase maps behave when the oven temperature changes and creates a gradient across the aperture, and how long does it take to these phases to stabilize once the oven temperature stops changing (time it takes for the gradient to disappear).

In February 2007, during an oven temperature transition from 30 to 35°C, about seven and a half hours of laser-light detune sequences were taken with HMI in the vacuum tank. These data show that the features on the phase maps of the tunable elements "drift" slowly across the element apertures before coming back to normal once the temperature is stabilized. Figure 21 shows three different sets of phase maps obtained for the tunable elements at three different unstable oven temperatures: 29.9°C, 31.3°C, and 32.0°C. In this case, it took less than the seven-hour run for the phase patterns to stabilize (probably around five hours, but sudden jumps in the dye-laser wavelength make it difficult to estimate more precisely the time of stabilization): this is more than the roughly three and a half hours it took for the oven temperature to reach 35°C. Therefore, thermal stability of the phase maps (and therefore transmission profiles) of the tunable elements is only reached several hours after the oven temperature stops changing.

4.2. Instrument Throughput

The overall throughput, or ratio of the transmitted to input intensity, of the instrument needs to be assessed to determine the appropriate exposure times. Four detune sequences were taken at LMSAL in sunlight and CALMODE in the course of a same day, at different times (to access different airmasses). To compute the throughput we calculate the attenuation of the incoming solar flux by the Earth atmosphere. We apply the Beer–Bougher–Lambert absorption law, assuming, among others, that the atmosphere is homogeneous:

$$\ln I_c = \ln I_{c0} - kX \tag{35}$$

where I_c is the solar continuum intensity obtained from the detune-sequence data by the fitting code mentioned in Section 3.3.1, I_{c0} is the quantity we need to derive (continuum intensity in the absence of atmospheric absorption/scattering, *i.e.* at airmass zero), k is the extinction coefficient at the solar line central wavelength, and X is the airmass (returned by an ephemeris). The four fitted I_c values have to be corrected for the changes in the ratio inside-LMSAL to outside-LMSAL sunlight intensities. These ratios were measured with a power meter before each detune sequence, and their difference is due to the heliostat mirrors. Using the previous equation, I_{c0} is obtained by extrapolation at airmass zero (see Figure 22). With the four detune sequences analyzed, the lowest airmass reached is only 1.16, and therefore the extrapolation result has a large uncertainty. The number of photo-electrons detected on a CCD pixel per second in the HMI passband and at airmass zero is estimated from I_{c0}, the gain of the CCD (here taken as 16.36 for the side camera, see Wachter *et al.*, 2010), and

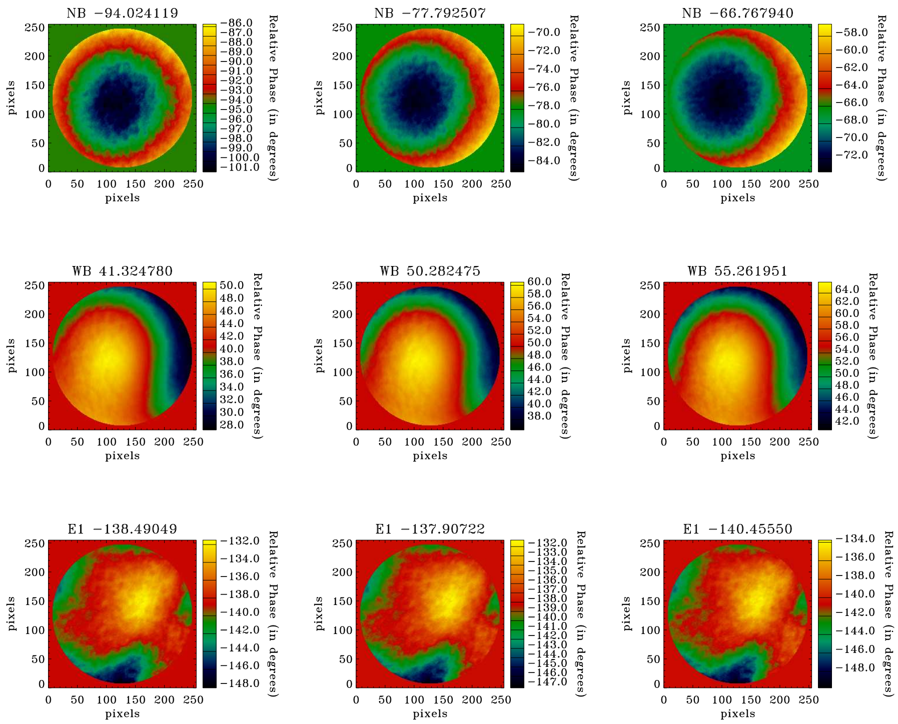

Figure 21. Change in the relative phases of the tunable elements during an oven temperature transition from 30 to 35°C. The numbers in the panel titles are the average phases for the NB, WB, and E1 elements. The left column is for an average oven temperature of 29.9°C; the central column is for 31.3°C; and the right column is for 32.0°C. Detune sequences in OBSMODE taken in vacuum in February 2007, at a laser wavelength of 6173.3046 Å (estimate).

the HMI sampling-position transmittances. The number of photons per second per pixel in the HMI passband, received at the entrance of the HMI instrument, is estimated from a black-body radiation law and the equivalent width of the HMI sampling-position transmittances. The ratio of these two quantities provides the throughput, here estimated at about 1.35%. This is on the low side of the expected range: a conservative radiometric analysis based on the specification numbers of the HMI components returns a low estimate of 1.15% for the throughput, and, considering that many components have efficiencies significantly exceeding their specifications, a tentative high estimate is about 2% (*e.g.* using 0.99 instead of 0.9 for all the mirror reflectivities). With a 1.35% throughput, the exposure time corresponding to an exposure level of 125 000 electrons (for a CCD full well of 150 000) is about 160 ms, much smaller than the maximum exposure time allowing the 45-second cadence required to produce the Doppler velocity maps.

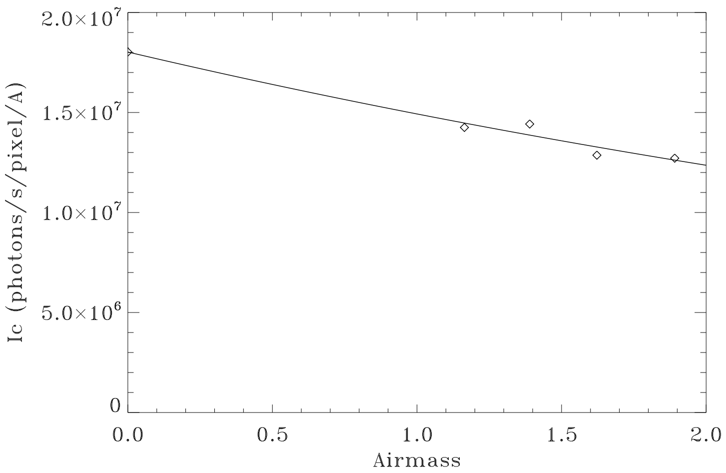

Figure 22. Measurement of the throughput of HMI: shown are the solar continuum intensities (in photons s^{-1} $pixel^{-1}$ $Å^{-1}$) derived as a function of the airmass from four detune sequences in CALMODE and sunlight taken during a single day of September 2007. The diamonds are the data points, except for the point at Airmass=0 which is extrapolated, while the solid line is the result of a fit using the Beer–Bougher–Lambert law of atmospheric absorption.

4.3. Artifact Check

It is necessary to check whether or not the fringe patterns produced by the front window and blocking filter, as well as the *I*-ripple value, vary with the focus blocks. This is the purpose of the artifact check test. To this end, detune sequences were taken in white light for focus positions 1 to 13 (OBSMODE). There was no significant difference in the fringe patterns and the value of the *I*-ripple. For instance, Figure 23 shows how stable this *I*-ripple is with respect to the focus blocks: the relative differences in intensities between detune sequences taken at seven different blocks are very small (maximum relative difference of 0.015%).

4.4. Tuning Polarizer Check

The two Michelson interferometers can be tuned by rotating a combination of a half-wave plate, a polarizer, and a second half-wave plate. Under normal conditions only the half-wave plates will be used. The tuning polarizer is a redundant mechanism: were one of the two wave plates to fail, we could still tune HMI. To check whether the tuning polarizer is working properly, we use a detune sequence with four extra positions added to the usual 27-position sequence: the HCM of the tuning polarizer is set at the angles $\phi = 30$, 60, 90, and 120° (corresponding to tuning phases of 60, 120, 180, and 240°). This detune sequence is taken with a laser as light source and in the presence of the stimulus telescope. We fit the sequence filtergrams for the laser relative intensity, and the phases and contrasts of the tunable elements. We then reconstruct the detune sequence. The reconstruction shows whether or not the polarizer is working: a poor reconstruction is

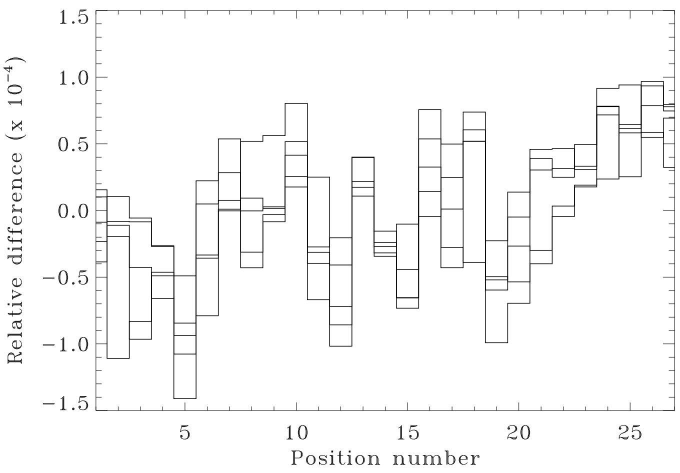

Figure 23. Artifact check for the *I*-ripple: relative differences in the spatially-averaged intensities of seven detune sequences taken with different focus blocks (1,2,3,4,5,9, and 13) in September 2007 with lamp light, in vacuum, and at an oven temperature of 29.5° C.

a sign of defect in the tuning polarizer. An example of such an analysis is shown on Figure 24. It confirms that the tuning polarizer is working as expected.

4.5. HMI Sampling-Position Profiles and the Computation of the Doppler Velocity and l.o.s. Magnetic-Field Strength

The results presented in this paper allow a derivation of the tuning-position transmission profiles used in the observable sequence. The nominal plan is that a HMI observable sequence will consist of filtergrams taken at six different tuning positions, roughly spanning the range $[-172.5, +172.5]$ mÅ around the target wavelength, and at different polarizations (Left Circular Polarization [LCP] and Right Circular Polarization [RCP] for the l.o.s. observables, or some combinations of the Stokes vector components I, Q, U, and V for the full vector magnetic field). The Doppler velocities and l.o.s. magnetic-field strengths will therefore be calculated using 12 filtergrams (six tuning positions, and two polarizations). At first, the algorithm converting the intensities on these filtergrams into l.o.s. observables will be based on the one used by MDI (see Scherrer *et al.*, 1995). Later, we plan to use a least-squares fit of an appropriate model of the Fe I line profile. The MDI-like algorithm is based on a discrete estimate of the first and second Fourier coefficients of the Fe I profile. The velocities corresponding to the phases, obtained by arctangent, of these Fourier coefficients are calculated. These velocities are then corrected using look-up tables. Correction is needed because the sampling-position transmission profiles are not delta functions. We only use six tuning positions to estimate the Fourier coefficients, and the formula applied to convert Fourier coefficients into Doppler velocities is only approximate (*e.g.*, it assumes that the solar line has a Gaussian profile). The look-up tables (two of them: one for the velocities returned by the first Fourier coefficient, and one for

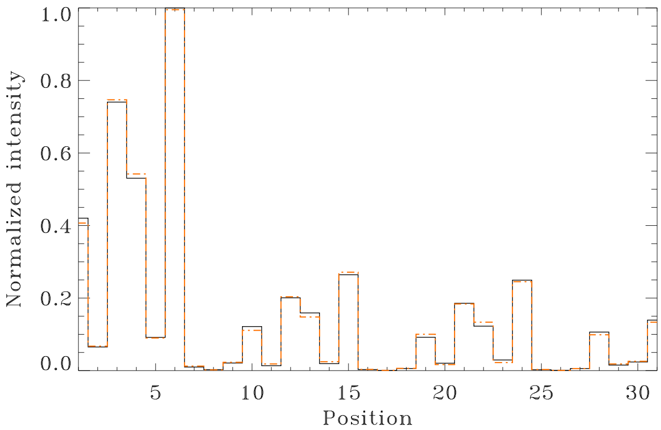

Figure 24. Reconstruction (in red and dashed line) of a spatially-averaged 31-position detune sequence (in black solid line), taken in October 2007 in OBSMODE. This sequence includes four different positions for the tuning polarizer (the last four). The reconstruction is based on phases and contrasts of the tunable elements that were fitted on the actual detune sequence. The good agreement between actual and reconstructed sequences confirms that the tuning polarizer is working properly.

the velocities returned by the second Fourier coefficient) are computed separately in a program based on the HMI sampling-position profiles derived from the results presented here, and based on profiles of the solar Fe I line that were provided by R. K. Ulrich at three angular distances from disk center (profiles publicly available as text files on http://hmi.stanford.edu/data/calib/ironline/). Figure 25 shows an example of six HMI sampling-position profiles at CCD center and their location with respect to the solar Fe I line at rest and at disk center (the zero wavelength corresponds to the target wavelength 6173.3433 Å).

4.6. Preliminary Plans for the On-Orbit Calibration

It is theoretically possible to improve and further our knowledge of the HMI-filter transmission profiles by using on-orbit calibration procedures. SDO will orbit the Earth in a geosynchronous orbit. The Sun–SDO radial velocity at any given time will be known with a high precision. This velocity should vary in the maximum range $\approx [-3.5, +3.5]$ km s^{-1} daily. The exact range changes during the year. We plan to use this velocity range to accurately determine the FSRs of the tunable elements, by taking series of detune sequences in CALMODE and OBSMODE at different times of a day. Rolls and offpoints may also be used.

Moreover, as previously mentioned, the l.o.s. observables will be determined from HMI filtergrams using a MDI-like algorithm based on six sampling positions. With this algorithm a set of look-up tables are computed, which are an estimate of the Doppler velocity returned by the algorithm as a function of the actual velocity, based on our knowledge of the sampling-function transmission profiles. Using the known Sun–SDO velocity and taking cotune sequences, it

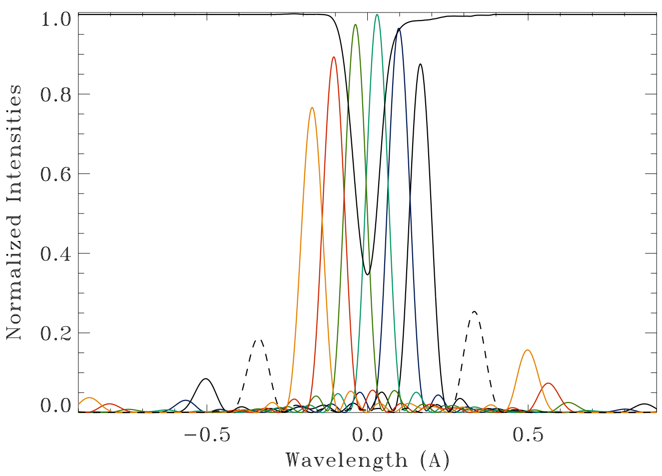

Figure 25. Example of HMI sampling-position profiles obtained from the wavelength-dependence calibration procedure (these profiles vary across the CCD and depend on the tuning angles used). Six tuning positions are shown here with respect to the Fe I solar line (black line) at disk center and at rest, on top of the continuum tuning position (dashed line). The continuum tuning position can be used to estimate the solar continuum intensity. The Fe I line profile was provided by R. K. Ulrich and obtained at the Mount Wilson Observatory.

is possible to check the accuracy of, and partly correct, these look-up tables. Therefore, it should be possible to account for some effects not modeled in the transmittance formulae (*e.g.* the *I*-ripples, the CALMODE-OBSMODE phase differences) and the Fe I line profile used. Finally, it will also be possible to monitor the drift with time in the wavelengths of peak transmittance of the Michelson interferometers.

5. Conclusion

A thorough investigation of the wavelength dependence of the HMI instrument was conducted during the course of years of calibration tests performed at the LMSAL facility in Palo Alto, and later at the NASA Goddard Space Flight Center in Maryland, and Astrotech Space Operations in Florida. The main results obtained on the assembled instrument are summarized in Table 5. Using various light sources (sunlight, laser light, lamp light) and a combination of detune and cotune sequences, it was possible to derive the transmittances of the elements of the HMI optical-filter system, their temperature dependence, and their angular dependence. These wavelength-calibration tests showed the very high quality of the HMI optical-filter system, and helped in detecting and correcting some defects. In particular, the early detection of a large *I*-ripple ($> 10\%$) was instrumental in highlighting a problem with the Lyot filter. This problem was successfully corrected. The knowledge of the transmission profiles of the filter elements is key to deriving accurate solar Doppler velocities and vector

Table 5. Summary of selected ground calibration results for tests performed on the assembled instrument.

Test	OBSMODE	CALMODE
phase gradient of NB	$\approx 16°$	$\approx 19°$
phase gradient of WB	$\approx 24°$	$\approx 29°$
phase gradient of E1	$\approx 16°$	$\approx 15°$
phase gradient of E2	$\approx 20°$	$\approx 18.5°$
phase gradient of E3	$\approx 20°$	$\approx 20°$
phase gradient of E4	$\approx 36.5°$	$\approx 36°$
phase gradient of E5	$\approx 30°$	$\approx 28°$
average contrast of NB	≈ 0.969	≈ 0.977
average contrast of WB	≈ 0.997	≈ 0.997
average contrast of E1	≈ 0.962	≈ 0.974
average contrast of E2	≈ 0.985	≈ 0.986
average contrast of E3	≈ 0.965	≈ 0.965
average contrast of E4	≈ 0.988	≈ 0.988
average contrast of E5	≈ 1.000	≈ 0.999
phase drift of NB	$0.2° - 0.43°$ per day	$0.2° - 0.43°$ per day
phase drift of WB	$\approx 0.15°$ per day	$\approx 0.15°$ per day
phase drift of E1	0	0
FSR of NB	≈ 170.9 mÅ	≈ 170.9 mÅ
FSR of WB	≈ 341.9 mÅ	≈ 341.9 mÅ
FSR of E1	≈ 693.5 mÅ	≈ 693.5 mÅ
total I-ripple	$\approx 1.9\%$	$\approx 1.9\%$
I-ripple of NB	$0.81 - 1.15\%$	$0.81 - 1.15\%$
I-ripple of WB	$0.78 - 0.99\%$	$0.78 - 0.99\%$
I-ripple of E1	$0.98 - 2.03\%$	$0.98 - 2.03\%$
angular dependence of NB at $\theta = 0.9°$	≈ 14 mÅ	≈ 14 mÅ
angular dependence of WB at $\theta = 0.9°$	≈ 8.5 mÅ	≈ 8.5 mÅ
angular dependence of E1 at $\theta = 0.9°$	$\approx 51 - 70$ mÅ	$\approx 51 - 70$ mÅ
temperature dependence of NB at 30° C	≈ -9.5 mÅ°C^{-1}	≈ -9.5 mÅ°C^{-1}
temperature dependence of WB at 30° C	≈ -9.7 mÅ°C^{-1}	≈ -9.7 mÅ°C^{-1}
temperature dependence of E1 at 30° C	≈ -12.4 mÅ°C^{-1}	≈ -12.4 mÅ°C^{-1}
throughput	not measured	$\approx 1.35\%$

magnetic fields. The Michelson interferometers have a high degree of spatial uniformity, with a phase range of 16° across the aperture for the NB Michelson (equivalent to a wavelength range of 7.6 mÅ, or a velocity range of 369 m/s), and 24° for the WB (equivalent to a wavelength range of 22.9 mÅ, or a velocity range of 1113 m/s). Similarly the Lyot tunable element E1 has a phase range of 16° (30.7 mÅ, or 1492 m/s). The contrasts of these tunable elements are also very high (larger than 0.96 on average). This compares favorably to the tunable elements of the MDI instrument onboard SOHO. The angular dependence of the tunable elements proved difficult to measure, and seems higher than expected for E1 (which also displays some azimuthal dependence). The maximum wavelength change of the transmission profile, compared to the profile for normal rays, was measured at $\theta = 0.9°$ for E1 and is larger than 50 mÅ. The angular dependence of the Michelsons appears much smaller. The temperature dependence of the tunable elements is relatively weak, less than -12.4 mÅ $°C^{-1}$ at the nominal oven temperature. The Michelson transmission profiles drift in wavelength over time, but the drift rate is expected to slow down with time. Each tunable element has less than 1% of I-ripple (E1 being the worst), which is a further proof of a very good manufacturing and assembly. The overall I-ripple is of the order of 1.9%. The non-tunable transmission profile was also characterized and the Lyot elements E2 to E5 are of high quality in terms of phase gradient and contrast. Finally, the throughput of the instrument is about 1.35%, resulting in an exposure time well below the maximum value allowing the 45-second cadence required to produce the l.o.s. observables.

Once SDO is orbiting the Earth, regular calibration tests will be performed to ensure that HMI is constantly providing the best observables possible. Moreover, the SDO-Sun radial velocity, known with a precision better than 1 m/s, will be used to, at least partly, correct for residual errors in the wavelength calibration.

Acknowledgements This work was supported by NASA Grant NAS5-02139 (HMI). We thank the HMI team members for their hard work, A. Title for providing us with notes regarding Jones calculus applied to the Lyot elements, and R.K. Ulrich for providing us with profiles of the solar Fe I line at 6173 Å. The HMI project is grateful to Karel Urbanek, Carsten Langrock, Joe Schaar and Robert Byer at Stanford University's Ginzton Laboratory for designing and building the tunable solid-state laser. We also thank Todd Hoeksema, Brett Allard, and countless others at LMSAL for their help with the taking of the calibration data. Finally, we acknowledge the comments of the anonymous referee for improving the quality of this article.

References

Dravins, D.: 1982, *Ann. Rev. Astron. Astrophys.* **20**, 61.
Dravins, D., Lindegren, L., Nordlund, A.: 1981, *Astron. Astrophys.* **96**, 345.
Evans, J.W.: 1949, *Opt. Soc. Am.* **39**, 229.
Gault, W.A., Johnston, S.F., Kendall, D.J.W.: 1985, *Appl. Opt.* **24**, 1604.
Norton, A.A., Graham, J.P., Ulrich, R.K., Schou, J., Tomczyk, S., Liu, Y., Lites, B.W., Ariste, A. Lopez, Bush, R.I., Socas-Navarro, H., Scherrer, P.H.: 2006, *Solar Phys.* **239**, 69.
Scherrer, P.H., Bogart, R.S., Bush, R.I., Hoeksema, J.T., Kosovichev, A.G., Schou, J., *et al.*: 1995, *Solar Phys.* **162**, 129.
Title, A.M.: 1974, *Solar Phys.* **39**, 505.
Title, A.M., Rosenberg, W.J.: 1979, *Appl. Opt.* **18**, 20, 3443.
Title, A.M., Ramsey, H.E.: 1980, *Appl. Opt.* **19**, 2046.
Title, A.M., Pope, T.P., Ramsey, H.E., Schoolman, S.A.: 1976, In: *Development of birefringent filters for spaceflight*, Lockheed Missiles and Space Co., Palo Alto, CA, publicly available on the NASA Technical Reports Server (document ID 19780011984)